

THE NEAR-INFRARED CO ABSORPTION BAND AS A PROBE TO THE INNERMOST PART OF AN AGN OBSCURING MATERIAL

SHUNSUKE BABA

Institute of Space and Astronautical Science, Japan Aerospace Exploration Agency, 3-1-1 Yoshinodai, Chuo-ku, Sagami-hara, Kanagawa 252-5210, Japan and
Department of Physics, Graduate School of Science, The University of Tokyo, 7-3-1 Hongo, Bunkyo-ku, Tokyo 113-0033, Japan

TAKAO NAKAGAWA

Institute of Space and Astronautical Science, Japan Aerospace Exploration Agency, 3-1-1 Yoshinodai, Chuo-ku, Sagami-hara, Kanagawa 252-5210, Japan

NAOKI ISOBE

Institute of Space and Astronautical Science, Japan Aerospace Exploration Agency, 3-1-1 Yoshinodai, Chuo-ku, Sagami-hara, Kanagawa 252-5210, Japan

MAI SHIRAHATA

Institute of Space and Astronautical Science, Japan Aerospace Exploration Agency, 3-1-1 Yoshinodai, Chuo-ku, Sagami-hara, Kanagawa 252-5210, Japan

(Received; Revised; Accepted)
Draft version April 20, 2022

ABSTRACT

We performed a systematic analysis of the 4.67 μm CO ro-vibrational absorption band toward nearby active galactic nuclei (AGNs) and analyzed the absorption profiles of ten nearby galaxies collected from the *AKARI* and *Spitzer* spectroscopic observations that show the CO absorption feature by fitting a plane-parallel local thermal equilibrium gas model. We found that CO gas is warm (200–500 K) and has a large column density ($N_{\text{H}} \gtrsim 10^{23} \text{ cm}^{-2}$). The heating of the gas is not explicable by either UV heating or shock heating because these processes cannot represent the large column densities of the warm gas. Instead, X-ray photons from the nuclei, which can produce large columns of warm gas with up to $N_{\text{H}} \sim 10^{24} \text{ cm}^{-2}$, are the most convincing power source. The hydrogen column density estimated from the CO band is smaller than that inferred from X-ray observations. These results indicate that the region probed by the near-infrared CO absorption is in the vicinity of the nuclei and is located outside the X-ray emitting region. Furthermore, the covering factors nearly unity required by the observed deep absorption profiles suggest that the probed region is close to the continuum source, which can be designated as the inner rim of the obscuring material around the AGN.

Subject headings: galaxies: active — galaxies: nuclei — infrared: galaxies

1. INTRODUCTION

Active galactic nuclei (AGNs) show a wide diversity of observational characteristics in their spectra. AGN spectra differ primarily in terms of optical broad emission lines, the presence or absence of which are used to classify the AGNs as types 1 or 2, respectively. This dichotomy has been attributed to a viewing angle effect caused by a putative AGN torus, an optically and geometrically thick torus-shaped dusty cloud that obscures direct emission from the nuclear region when the AGN is viewed edge-on (AGN unified model, Antonucci 1993). To understand the characteristics of AGNs, it is important to observe AGN tori and verify the AGN unified model. However, because of their small sizes on parsec scales, it is difficult to directly image AGN tori. Recent millimeter to sub-millimeter interferometric observations with the Atacama Large Millimeter Array of carbon monoxide (CO) pure rotational emission lines revealed the presence of gas concentrated near central nuclei (e.g., García-Burillo et al. 2016), but the highest spatial resolution that can be achieved with such observations is about several parsecs,

even in the nearest AGNs. Thus, in distant galaxies millimeter and sub-millimeter emission lines are not suitable for resolving AGN tori from their hosts. An alternative observing method that can be applied to large numbers of AGNs is required.

The strategy we employ in this paper is based on spectroscopy of the CO fundamental ro-vibrational absorption band centered at 4.67 μm ($v = 1 \leftarrow 0$, $\Delta J = \pm 1$). Using the bright near-IR radiation from the central region as the background continuum, this technique can observe foreground molecular gas clouds with an effectively high spatial resolution at the parsec scale because of the compactness of the near-IR emitting region. Furthermore, because this band contains multiple lines with different rotation levels in a narrow wavelength range, it is possible to obtain information on the gas excitation state from one observation. In this respect, the near-IR CO absorption band is preferable to the (sub-)millimeter CO pure rotational emission lines, which are easily affected by contamination from the host galaxy and cannot be observed simultaneously.

Geballe et al. (2006) and Shirahata et al. (2013, hereafter S13) observed the absorption band toward the heavily obscured ultra-luminous infrared galaxy (ULIRG) IRAS 08572+3915 using the United Kingdom 3.8-m Infrared Telescope (UKIRT) and the 8.2-m Subaru telescope, respectively. Strong absorption lines were detected up to high rotational levels ($J \leq 17$), with the resulting population diagram showing the presence of large columns of warm molecular gas in the line of sight. Spoon et al. (2004, hereafter S04) observed another obscured ULIRG IRAS 00182–7112 using the *Spitzer Space Telescope* and also detected strong CO absorption. Although their observation did not resolve the multiple lines owing to insufficient spectral resolution, they analyzed the entire absorption profile using a plane-parallel local thermal equilibrium (LTE) gas model (Cami 2002) and also found that the gas is warm and has a large column density. Based on the high temperatures and large column densities, both authors argued that the observed gas should be in the vicinity of the dominant nuclear power source. S13 also proposed that the warm gas is heated by X-ray radiation from an AGN engine.

This CO absorption feature, however, does not always appear in all type-2 AGNs, in which the putative torus should be seen edge-on. Lutz et al. (2004) observed nearby 19 Seyfert 1 (Sy1) and 12 Seyfert 2 (Sy2) galaxies using *Infrared Space Observatory* (ISO), but none showed the CO feature. Lahuis et al. (2007) detected similar warm molecular gas toward obscured (U)LIRGs through the mid-IR absorption bands of C_2H_2 , HCN, and CO_2 but concluded that the gas is unlikely to be associated with the material surrounding AGNs because these molecules would be rapidly destroyed in an intense X-ray field. The two above studies controvert the hypothesis that CO absorption probes warm gas near the central region.

To assess the location of the region probed by CO rovibrational absorption, in this study we analyzed space telescope observations of the CO feature toward ten nearby AGNs and compared the results with the results from other X-ray and mid-IR observations. Such a systematic analysis of the CO absorption profile had not previously been performed, although detection of the feature has been reported in some objects (Imanishi et al. 2008, 2010; Spoon et al. 2005). Together with a description of observations and data reduction, the selection of our targets is explained in Section 2. The method used to analyze the CO absorption profile is described in Section 3, followed by presentation of results in Section 4. We discuss these results and compare them with other observations in Section 5 and, finally, we give our conclusion in Section 6.

2. TARGETS, OBSERVATIONS, AND DATA REDUCTION

We used spectroscopic observations carried out with the *AKARI* satellite (Murakami et al. 2007) and the *Spitzer Space Telescope* (Werner et al. 2004) to collect targets that show CO absorption. *AKARI* and *Spitzer* have near- and mid-IR spectrometers, respectively, which cover complementary redshift ranges. Because we were not able to obtain information on the longward continuum level over the CO absorption from the *AKARI* observations themselves, *Spitzer* data were used to com-

plement the spectrum in longer wavelengths. For these sources, we scaled the two spectra using *WISE* catalog magnitudes as reference points. In the following, we describe in detail the observations and data reduction techniques and present the spectra of the targets.

2.1. *AKARI*

We searched AGNs showing CO absorption from the archival data of the *AKARI* mission program AGNUL (P.I. T. Nakagawa). The program conducted many spectroscopic observations of nearby AGNs and ULIRGs using the Infrared Camera (IRC) in the NG grism mode. Almost all of the observations were performed through a $1' \times 1'$ aperture, and thus constituted slitless spectroscopy. The NG grism mode covers a wavelength range from 2.5 to 5.0 μm . Although its spectral resolution in general depends on the spatial extent of the target, if it is a point source, the resolution can be given as $R = 33.3\lambda$, where λ is the observed wavelength in μm (Onaka et al. 2007; Ohyama et al. 2007). The redshift range within which it is possible to observe the band center of the CO feature is $z < 0.07$. The AGNUL program also carried out observations in another dispersion mode (NP), but we excluded these from our sample because the spectral resolution of that mode was insufficient for the following analysis. The observation period of the program is divided into two parts: a cryogenic phase and a post-cryogenic phase. In this study, we scoped only cryogenic observations, which had been calibrated better than the post-cryogenic observations. A study using post-cryogenic data will be presented in a forthcoming paper.

Under the above conditions, 50 ULIRGs were observed, eight of which are within $z < 0.07$. We found that the six ULIRGs listed in the upper part of Table 1 show CO absorption. The other two ULIRGs are Mrk 231 and IRAS 05189–2524, which are classified as Sy1 and Sy2, respectively (Veilleux et al. 1995). Table 1 also presents the redshift, optical classification, and IR and X-ray AGN signatures of the six CO ULIRGs. Although some of these are not classified as Seyferts, either IR or X-ray diagnostics suggest that they are AGN hosts, and we therefore assumed that all six ULIRGs harbor an AGN and used them as targets for analysis. IRAS 23128–5919 is a merging system with a nuclear separation of $5''$ (Duc et al. 1997). The southern nucleus of the galaxy was detected in hard X-rays with *Chandra* and believed to be an obscured AGN based on the observed X-ray hardness ratio (Iwasawa et al. 2011).

Table 2 summarizes observational information obtained from *AKARI*/IRC. In the NG mode, a spectrum is contaminated by second-order light at wavelengths longer than 4.9 μm . A correction for this effect was established by Baba et al. (2016), whom we followed in performing data reduction. One-dimensional raw spectra were extracted using the official IRC Spectroscopy Toolkit Version 20150331 in the standard manner. To minimize uncertainty in the wavelength calibration, the wavelength origin was adjusted from the value reported by the toolkit by a few pixels based on the positions of features such as the 3.3 μm PAH emission band, H I Br α and Br β emission lines, and 4.26 μm CO_2 absorption band. The wavelength dependence of the refractive index of the grism material was included in the wavelength cali-

TABLE 1
BASIC TARGET DATA

Group	Object	z	$\log L_{\text{IR}}$ (L_{\odot})	Optical Class	AGN Sign		Ref.
					IR	X-ray	
<i>AKARI</i>	IRAS 06035–7102	0.0797	12.2	LI	✓	...	1; 6, 7; —
	IRAS 08572+3915	0.0583	12.1	LI	✓	✓	2, 3; 7, 8; 9
	UGC 5101	0.0392	12.0	LI	✓	✓	3; 7, 8; 9
	Mrk 273	0.0373	12.2	Sy2	✓	✓	2, 3; 6, 7; 9
	IRAS 19254–7245	0.0616	12.1	Sy2	✓	✓	1, 4; 7, 8; 10
	IRAS 23128–5919	0.0448	12.0	H II/Sy2/LI	—	✓	1; 6; 9
<i>Spitzer</i>	IRAS 00182–7112	0.3270	12.9	LI	✓	✓	5; 8; 11
	IRAS 00397–1312	0.2617	13.0	H II	✓	—	2; 8; 12
	IRAS 00406–3127	0.3424	12.8	Sy2	✓	...	4; 7; —
	IRAS 13352+6402	0.2366	12.5	?	✓	...	—; 7; —

NOTE. — Column 1: target group. Column 2: object name. Column 3: redshift taken from the PSCz catalog (Saunders et al. 2000). Column 4: logarithm of the infrared (8–1000 μm) luminosity in units of the solar luminosity L_{\odot} derived from Sanders & Mirabel (1996): $L_{\text{IR}} = 2.1 \times 10^{39} \times D_L^2 \times (13.48 f_{12} + 5.16 f_{25} + 2.58 f_{60} + f_{100}) \text{ erg s}^{-1}$, where D_L is the distance in Mpc, and f_{12} , f_{25} , f_{60} , and f_{100} are *IRAS* fluxes in Jy. In calculating D_L , $H_0 = 70 \text{ km s}^{-1} \text{ Mpc}^{-1}$, $\Omega_m = 0.3$, and $\Omega_{\Lambda} = 0.7$ are adopted. The *IRAS* fluxes are taken from Sanders et al. (2003), Kim & Sanders (1998), or the *IRAS* Faint Source Catalog Version 2.0. For objects having upper limits in the *IRAS* fluxes, we evaluated the upper and lower limits of L_{IR} by assuming an actual flux equal to the upper limit and a zero value, respectively. Those upper and lower limits are quite close, with a difference less than 0.16 dex. Ultimately, the average of the two limits was adopted. Column 5: optical spectral classification. “LI”, “Sy2”, “H II”, and “?” denote LINER, Seyfert 2, H II region, and no optical classification, respectively. Columns 6 and 7: IR and X-ray AGN signatures, respectively. Check: present. Dash: absent. Dots: no data. The IR signature is based on the low equivalent widths of the 3.3 and/or 6.2 μm PAH emissions. The X-ray signature is based on a hard photon index and/or strong iron K lines. Column 8: references for columns 5, 6, and 7 with semicolons as delimiters. 1: Duc et al. (1997). 2: Veilleux et al. (1999). 3: Veilleux et al. (1995). 4: Allen et al. (1991). 5: Armus et al. (1989). 6: Imanishi et al. (2010). 7: Sargsyan et al. (2011). 8: Imanishi et al. (2008). 9: Iwasawa et al. (2011). 10: Braito et al. (2009). 11: Nandra & Iwasawa (2007). 12: Nardini & Risaliti (2011).

TABLE 2
AKARI/IRC OBSERVATION LOG

Object	Observation ID	Observation Date
IRAS 06035–7102	1100130.1	2007 Mar 11
IRAS 08572+3915	1100049.1	2006 Oct 26
UGC 5101	1100134.1	2007 Apr 22
Mrk 273	1100273.1	2007 Jun 8
IRAS 19254–7245	1100132.1	2007 Mar 30
IRAS 23128–5919	1100294.1	2007 May 10

bration. Contamination from the second-order light was correctly removed in the flux calibration. Because the southern and northern parts of IRAS 23128–5919 were barely resolved in the two-dimensional spectral image, we selectively extracted flux from the southern part, which is known to be an AGN host as mentioned above. IRAS 06035–7102, IRAS 08572+3915, Mrk 273, and IRAS 19254–7245 also have double disks or nuclei, which we were not able to resolve because they either have small separations or are aligned in the dispersion direction of the two-dimensional spectral images.

2.2. *Spitzer*

Spoon et al. (2005) reported that four ULIRGs observed with the Infrared Spectrometer (IRS) onboard *Spitzer* (Houck et al. 2004) show CO absorption. The lower part of Table 1 presents basic information on these four ULIRGs. These ULIRGs are, except for IRAS 00406–3127, not optically classified as Seyferts but show IR AGN signatures. Thus, we investigated these ULIRGs in addition to the *AKARI* targets. The *Spitzer* targets

TABLE 3
Spitzer/IRS OBSERVATION LOG

Object	AOR Key	Observation Date
IRAS 06035–7102 W	4969728	2004 Apr 14
IRAS 08572+3915 NW	4972032	2004 Apr 15
UGC 5101	4973056	2004 Mar 23
Mrk 273	4980224	2004 Apr 14
IRAS 19254–7245 S	12256512	2005 May 30
IRAS 23128–5919 S	4991744	2004 May 11
IRAS 00182–7112	7556352	2003 Nov 14
IRAS 00397–1312	4963584	2004 Jan 4
IRAS 00406–3127	12258816	2005 Jul 11
IRAS 13352+6402	12258560	2005 Mar 20

are systematically more luminous than the *AKARI* targets. Table 3 summarizes the *Spitzer*/IRS observational information and tabulates the observations used to complement the spectra of the *AKARI* targets.

The spectra around the CO absorption were obtained in the IRS SL2 mode, which covers wavelengths from 5.21 to 7.56 μm with a spectral resolution $R = 16.5\lambda$ at a slit width of 3''6 (IRS Instrument Team and Science User Support Team 2011). This wavelength range corresponds to the redshift range $z = 0.12$ – 0.62 . The spectral resolution is lower than that of the *AKARI*/IRC NG mode but sufficient for the following analysis. The calibrated *Spitzer* spectra of the targets were downloaded from the IRS Enhanced Products on the *Spitzer* Heritage Archive.

2.3. Scaling to the WISE Photometry

Because the *AKARI*/IRC spectra of the *AKARI* targets lacked the longward part of the CO absorption owing to redshift, we supplemented them with *Spitzer*/IRS ones to estimate the longward continuum levels. To reduce the effect of the different aperture sizes of *AKARI* and *Spitzer*, we scaled the fluxes of the two spectra so that they match with the *WISE* photometry (Wright et al. 2010). The procedure was as follows. Profile-fit magnitudes were taken from the AllWISE catalog and converted into fluxes in Jy based on the zero magnitudes presented by Jarrett et al. (2011), with color corrections taken into account. The color correction factor for the *W1* band was calculated by integrating the product of the *AKARI* spectral response function and the relative shape of the *AKARI* spectrum, and those factors for the *W3* and *W4* bands were similarly obtained using the relative shape of the *Spitzer* spectrum. The *W2* band flux cannot put clear constraint because the band protrudes from the *AKARI* wavelength coverage. We thus evaluated only the lower limit for the factor, which resulted in the flux upper limit. The *AKARI* spectrum was scaled so that its flux density at the isophotal wavelength of the *W1* band ($\lambda_{\text{obs}} = 3.35 \mu\text{m}$) hits the color-corrected *W1* flux, and confirmed not to pass over the *W2* upper limit. The *Spitzer* spectrum was scaled so that its flux densities at the *W3* and *W4* isophotal wavelengths ($\lambda_{\text{obs}} = 11.56, 22.09 \mu\text{m}$) fit the corrected fluxes of the two bands.

After the scaling, the two spectra agreed well so that we were able to draw baselines smoothly (Section 3.1). The obtained combined spectra are shown in Figure 1. The resultant scaling shifts from the original fluxes were mainly within 20%, although the shift for the *Spitzer* spectrum of IRAS 23128–5919 was +64%. This large shift can be attributed to the compensation of the flux from the northern nucleus, which did not fall in the *Spitzer* slit but blends into the *AKARI* spectral extraction.

While the original flux uncertainties of the *AKARI* and *Spitzer* spectra were propagated into the combined spectra, the scale factor uncertainties were not, because only the continuum-normalized spectra were used in the analysis described below. However, the uncertainty in the ratio between the two scale factors, which affects the determination of the longward continuum level from the *Spitzer* spectrum, should be treated as a systematic error. The largest uncertainty in the ratio of the two scale factors was obtained in IRAS 23128–5919, in which the uncertainty was ± 0.11 out of 1.54. We estimate the systematic error stemming from this uncertainty in Section 4.

Figure 2 shows the *Spitzer* spectra of the four *Spitzer* targets. In contrast to the *AKARI* spectra of the *AKARI* targets, these spectra entirely cover the CO absorption within themselves. We did not apply any scaling to these spectra because the absolute fluxes were not important, as only the continuum-normalized spectra were used in the analysis.

3. ANALYSIS

3.1. Continuum-Normalized Spectra

We normalized each spectrum around the CO absorption with a continuum level estimated as a cubic spline curve interpolated between the pivots at 4.15, 4.35, 5.10,

and 5.40 μm . These pivots were taken so that they avoided the Bra line at 4.05 μm , CO₂ absorption at 4.26 μm , and PAH emissions at 5.27 and 5.70 μm (Smith et al. 2007). In IRAS 13352+6402, we used instead a quadratic continuum that passes over the remaining three pivots, as its spectrum did not cover wavelengths shorter than 4.21 μm . Figure 3 shows the adopted continuum curves and the resulting normalized spectra. In this figure, double-branched features are observed, with the branches at the long and short wavelength sides representing the *P*- and *R*-branches, respectively. The depth of the absorption is deep, and the width of each branch is broad ($\sim 0.2 \mu\text{m}$) compared to that observed toward Sgr A* ($\sim 0.05 \mu\text{m}$, Lutz et al. 1996). These characteristics suggest that the CO gas has a large column density and a high temperature of up to ~ 500 K.

3.2. Gas-Model Fitting

We used the plane-parallel LTE gas model developed by Cami (2002) to analyze the absorption profile. For simplicity, we assume that the CO gas comprises of a single component with uniform number density, temperature, and turbulent velocity (velocity width). We did not include any isotopomers other than ¹²C¹⁶O. The model gives the flux normalized to the background intensity, including the contribution of both the absorption by the gas and the thermal emission from the gas itself. Because the observed absorption profiles suggested high gas temperatures, to accurately take the relative contribution of the gas in emission compared to the continuum into account, we needed to explicitly assume the temperature of the background radiation source. Assuming that the background continuum source is an optically thick hot dust sublimation layer, we set the continuum as a blackbody $I_{\nu,0} = B_{\nu}(T_{\text{BG}})$ with a sublimation temperature $T_{\text{BG}} = 1500$ K (Barvainis 1987). The intensity we observe, I_{ν} , is then the sum of the absorbed background, $I_{\nu,0}e^{-\tau_{\nu}}$, and the emission from the CO gas itself, $B_{\nu}(T_{\text{CO}})(1 - e^{-\tau_{\nu}})$, where τ_{ν} is the optical depth of the CO gas, and T_{CO} is the gas temperature. Accordingly, the continuum-normalized intensity becomes

$$I_{\nu}/I_{\nu,0} = e^{-\tau_{\nu}} - \frac{B_{\nu}(T_{\text{CO}})}{B_{\nu}(T_{\text{BG}})} (1 - e^{-\tau_{\nu}}). \quad (1)$$

The optical depth for a transition $(v, J) = (0, J'') \rightarrow (1, J')$ at frequency ν_0 can be written as

$$\tau_{\nu} = N_{\text{CO}} \frac{h\nu_0}{4\pi} g_{J''} B_{J''J'} \frac{e^{-E_{J''}/kT_{\text{CO}}}}{Z(T_{\text{CO}})} \times \left(1 - e^{-h\nu_0/kT_{\text{CO}}}\right) \phi(\nu, \nu_0), \quad (2)$$

where N_{CO} is the total CO column density, $g_{J''} = (2J'' + 1)$ and $E_{J''}$ are the statistical weight and the energy level of the lower state, respectively, $B_{J''J'}$ is the Einstein coefficient of the transition, $Z(T_{\text{CO}})$ is the partition function at T_{CO} , and $\phi(\nu, \nu_0)$ is a line profile. We assumed a Gaussian profile for each transition with a common turbulent velocity v_{turb} :

$$\phi(\nu, \nu_0) = \frac{1}{\sqrt{\pi}\Delta\nu_{\text{D}}} e^{-(\nu-\nu_0)^2/\Delta\nu_{\text{D}}^2}, \quad (3)$$

$$\Delta\nu_{\text{D}} = \frac{v_{\text{turb}}}{c} \nu_0. \quad (4)$$

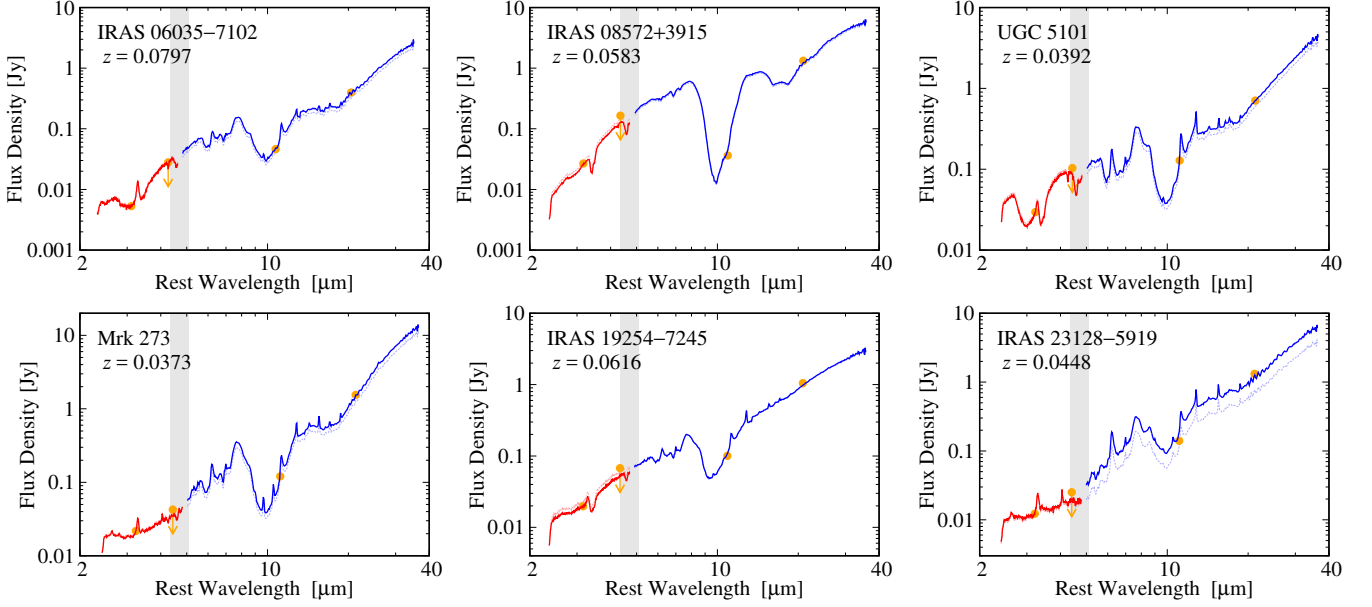


FIG. 1.— Combined spectrum of each *AKARI* target. Red and blue solid curves are the *AKARI*/IRC and *Spitzer*/IRS spectra scaled to match the *WISE* photometry, respectively (see text). Dashed lines in light colors, which are sometimes hidden behind the solid lines, are the original spectra before scaled. Orange filled circles represent the *WISE* photometric fluxes. The *AKARI* and *Spitzer* spectra are scaled so that they fit with the *WISE* points, but the W2 band ($4.6 \mu\text{m}$ in the observed frame) flux shown with a downward arrow is used only as an upper limit. Gray shaded areas indicate the wavelength range in which the CO absorption appears.

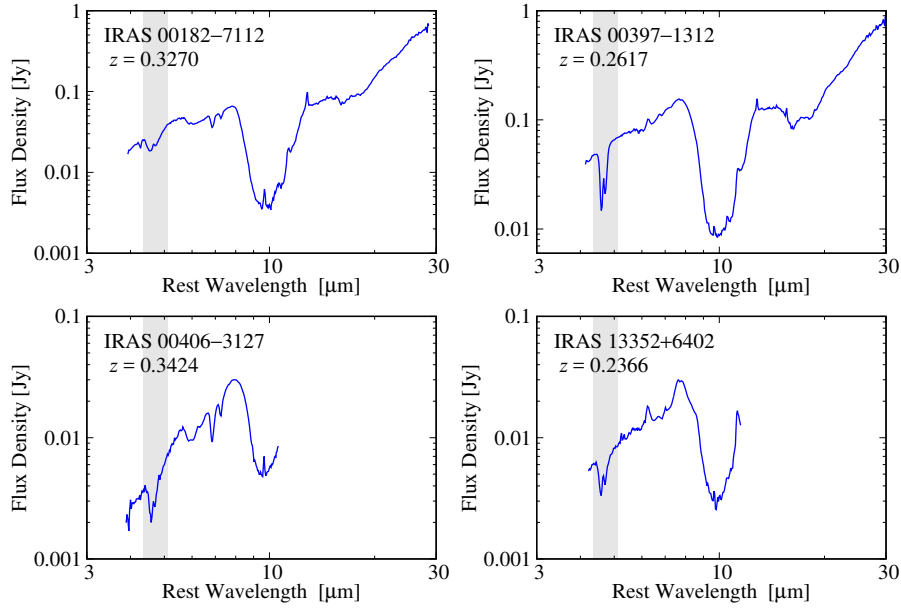


FIG. 2.— *Spitzer*/IRS spectrum of each *Spitzer* target (blue solid curves). Gray shaded areas indicate the wavelength range in which CO absorption appears.

From these equations, the intrinsic model spectrum can be parameterized by three variables: column density N_{CO} , temperature T_{CO} , and velocity width v_{turb} .

We can fit the model (Equation 1) to the data using N_{CO} , T_{CO} , and v_{turb} as free parameters, after convolving it with the instrumental spectral resolutions. The three parameters are somewhat degenerate with each other at such low resolutions since different rotational levels are not resolved, and the absorption spectrum is smoothed-out as a double-branched profile as observed in the previous subsection. Appendix A explains how the param-

eters alter the absorption profile.

Because most of the targets show absorption dominated spectra, the contribution from emission lines within the CO band can be generally expected to be small. However, there is some concern. The $\text{Pf}\beta$ line at $4.65 \mu\text{m}$ may be superimposed over the CO absorption. The theoretical line ratio of $\text{Pf}\beta/\text{Br}\alpha$ is 0.20 under the Case B condition, with $n_e \sim 10^2\text{--}10^7 \text{ cm}^{-3}$ and $T_e \sim (3\text{--}30) \times 10^3 \text{ K}$ (Storey & Hummer 1995). Considering the small equivalent width of the $\text{Br}\alpha$ line, we ignored the contribution from $\text{Pf}\beta$ in all the targets except for Mrk

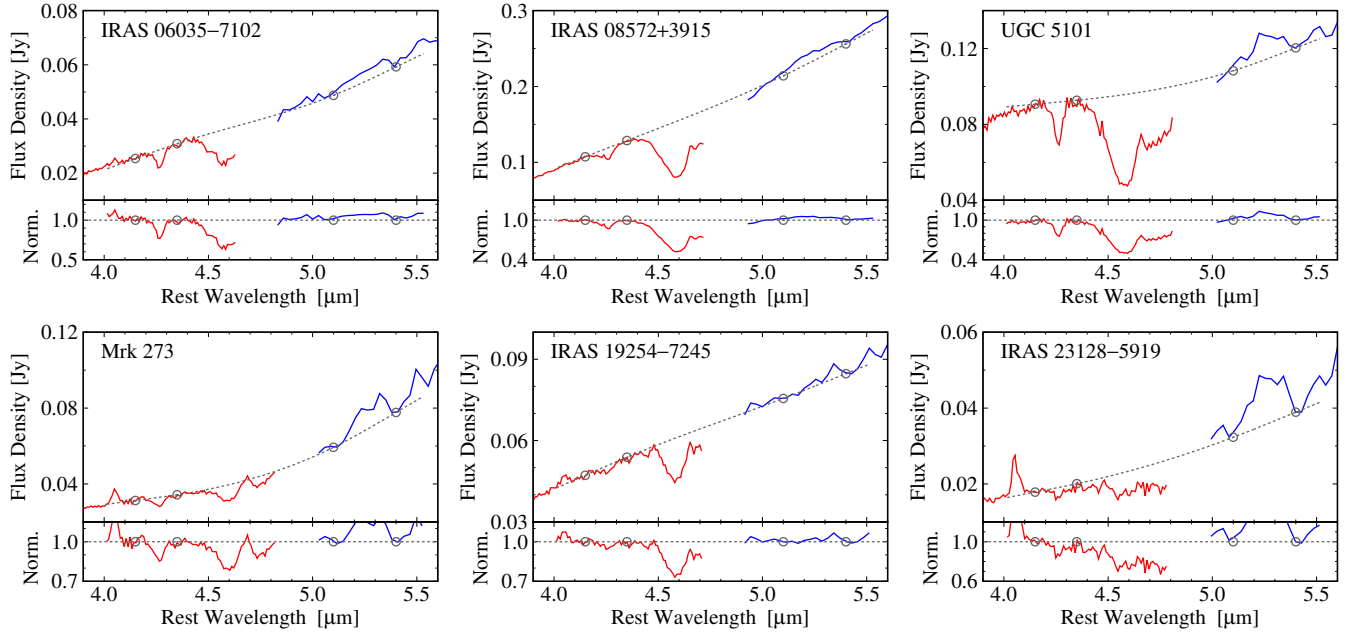


FIG. 3.— Continuum curves over the CO absorption (top) and continuum-normalized spectra (bottom). Red and blue curves are the *AKARI* and *Spitzer* spectra, respectively. Flux uncertainty is not shown here but is indicated in Figure 4. The continuum spectrum of each target (gray dotted line) is taken as a cubic spline curve that passes four pivots at 4.15, 4.35, 5.10, and 5.40 μm (gray open circles), except for IRAS 13352+6402, whose continuum is taken as a quadratic curve that passes the three pivots at longer wavelengths.

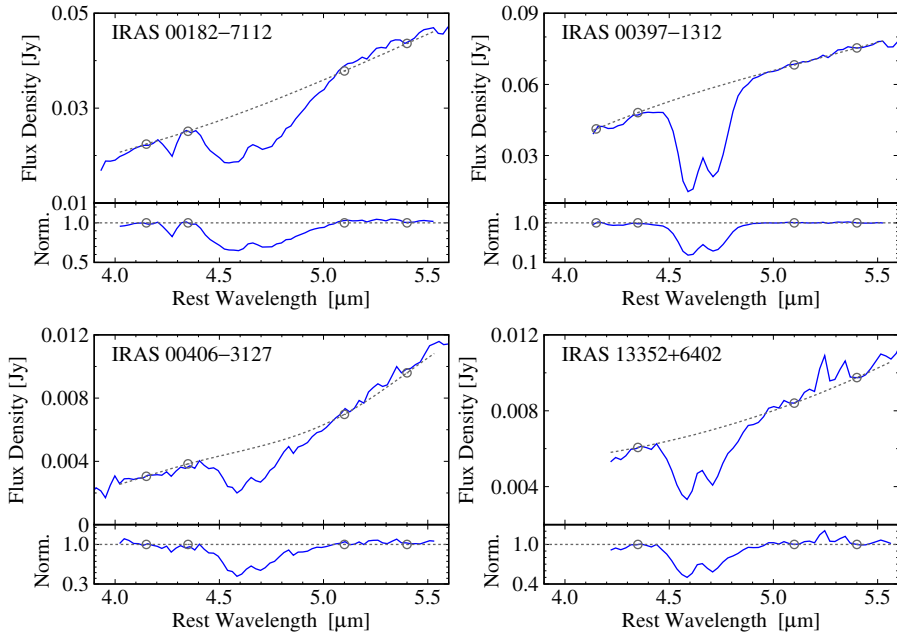


FIG. 3.— (Continued)

273, in which the observed intensity near the CO band center exceeded unity. Yano et al. (in preparation) found that this galaxy shows an anomalous $\text{Br}\beta/\text{Br}\alpha$ ratio in the *AKARI* spectrum. Accordingly, we attributed the high intensity to the effect of $\text{Pf}\beta$ and masked the data points within the $\pm 3\sigma$ wavelength range around that line assuming a line width at FWHM = 0.03 μm and excluded those points from the fitting process. There is no other H I line predicted to be stronger than the $\text{Pf}\beta$ line.

Another possible contamination is the molecular hy-

drogen pure-rotational line H_2 0–0 $S(9)$ at 4.69 μm . We estimated its flux from those of H_2 0–0 $S(7)$ at 5.51 μm and $S(3)$ at 9.66 μm . We did not use the $S(6)$, $S(5)$, and $S(4)$ lines at 6.11, 6.91, and 8.03 μm , respectively, because they can be blended with PAH emissions. On the assumption that $J = 5, 9$, and 11 levels are in LTE, the $S(9)$ line peak is derived to be smaller than 4% of the continuum level at 4.69 μm in all the galaxies. We thus ignore the contribution of the $S(9)$ line.

There are some fine structure lines that possibly appear over the CO band: $[\text{Mg IV}]$ 4.49 μm , $[\text{Ar VI}]$ 4.53 μm ,

and [Na VII] 4.69 μm . These transitions start from high excitation stages of 80, 75, and 172 eV, respectively, and, in Seyfert galaxies, usually observed to be weaker than the [Mg V] 5.61 μm line, whose excitation potential is 109 eV (Lutz et al. 2000; Sturm et al. 2002). We did not significantly detect the [Mg V] line above the 3σ level in all the targets. Hence we ignored any contribution from the three lines.

4. RESULTS

We derived the best-fit models using an iterative least-square method and confirmed that their solutions definitely provided the minimum χ^2 values through grid calculation. In the computation of the χ^2 values, uncertainties in the normalized flux of the data points were taken into account. In IRAS 00397–1312 and 13352+6402, because the observed data points appeared to be systematically displaced to shorter wavelengths from the best models we obtained at first, we manually shifted the points of the two galaxies by 0.009 and 0.010 μm , respectively, and then again fitted the model. These amounts are about the same as the wavelength calibration accuracy in the SL2 order of the IRS spectrum (0.008 μm RMS, IRS Instrument Team and Science User Support Team 2011). After this shifting, the reduced chi-squares for the two galaxies improved from 23.99 to 7.88 and from 7.14 to 3.39, respectively.

Figure 4 shows the best-fit CO gas model for each galaxy, and Table 4 tabulates the best-fit parameters and their 90% joint confidence ranges. A set of color maps of the $\Delta\chi^2$ value is shown in Appendix B. The fitting process returned quite high reduced χ^2 values ($\chi^2_{\nu} \equiv \chi^2/\text{dof}$). We consider that these poor fits originate from the difficulty in determining the continuum levels over the broad CO band. Some other possibilities concerning limitations of the current model are discussed in Section 5.1. We speculate that there is a systematic trend in which the observed flux in the red wing of the *P*-branch is higher than the model prediction; possible origins of this trend are also discussed in Section 5.1. The CO absorptions in IRAS 00182–7112 and IRAS 08572+3915 were also analyzed by S04 and S13, respectively. Comparisons between their results and ours appear in Appendix C.

We found that the observed CO gas has a high temperature and large column density. The average T_{CO} is 360 K, which is far higher than the typical temperature of molecular gas in ordinary star-forming regions (10–10² K, Hollenbach & Tielens 1999). The logarithm of N_{CO} in units of cm^{-2} is on average 19.5,¹ which corresponds to a molecular hydrogen column density of $\log N_{\text{H}_2} \sim 23.5$ if a CO abundance $[\text{CO}]/[\text{H}_2] = 10^{-4}$ is adopted. This large column density can be converted to extinction at *M*-band (5 μm) of $A_M \sim 8$ if we assume $N_{\text{H}} = 2N_{\text{H}_2}$ and Galactic relations $N_{\text{H}}/A_V = 1.9 \times 10^{21} \text{ cm}^{-2} \text{ mag}^{-1}$ (Bohlin et al. 1978) and $A_V/A_M \sim 40$ ($R_V = 3.1$, Draine 2003). Because we were able to observe CO gas absorption with this large column density, the extinction by dust must not be too high. This could suggest that the dust-to-gas ratio in AGN neighborhoods is lower than the Galactic value.

¹ Throughout this paper, the logarithm of column density is presented in units of cm^{-2} .

Note that the estimate of A_M have a major uncertainty depending on the assumption of the abundance ratio. The ratio measured in Galactic objects differs in $(0.8-3) \times 10^{-4}$ (Dickman 1978; Frerking et al. 1982; Watson et al. 1985; Black et al. 1990; Lacy et al. 1994). There is no direct measurement of the CO abundance in ULIRGs, to our knowledge. The range of the abundance leads $3 < A_M < 10$.

For the results of the *AKARI* targets, we estimated the systematic error stemming from the scaling of the *AKARI* and *Spitzer* spectra. In IRAS 23128–5919, the ratio of the scaling factor for the *Spitzer* spectrum to that for *AKARI* was determined to be 1.54 ± 0.11 ; this uncertainty was the largest among all the *AKARI* targets (Section 2). Changing the amount of scaling by this uncertainty, the fitting result of this galaxy differs by $\Delta(\log N_{\text{CO}}) \sim 0.2$, $\Delta T_{\text{CO}} \sim 40 \text{ K}$, $\Delta v_{\text{turb}} \sim 2 \text{ km s}^{-1}$. We therefore estimate that the systematic error is smaller than these values and conclude that this error does not affect the following discussion.

5. DISCUSSION

5.1. Limitations of the Current Model

As the model simplifies the CO gas temperature to a uniform value, the results should be treated as first order approximations. Here, we note some effects that are not incorporated in the current approximation.

If there are two or more temperature components, the higher-temperature components will make the column density appear to be larger. Under the current spectral fitting, the band wings strictly constrain the solution. The higher-temperature components work to lower the flux in the band wings in an effect similar to that of increasing the column density (see also Appendix A). The high reduced χ^2 values we obtained in the fitting may therefore be the result of over simplification of multi-temperature components. Although this factor is of concern, given the quality of the *AKARI* and *Spitzer* spectra, it is difficult to fit a more complicated multi-temperature gas model.

If there is an optically-thin foreground dust screen in front of the CO gas, as shown Figure 5(a), its thermal radiation will fill up the absorption. The observed potential trend in the shallow red wing of the *P*-branch (Section 4) may be caused by this effect. Similarly, if the CO gas extends to a larger solid angle than the continuum source as shown in Figure 5(b), the band profile would be skewed, as the outer part of the CO gas contributes merely by emission without absorbing the background light. This effect can be quantified in terms of the area ratio, f , of the CO gas to the background source. We can introduce f into Equation (1) by multiplying it with the second term. The increase of the normalized flux density owing to f is larger at longer wavelengths because $B_{\nu}(T_{\text{CO}})$ is redder than $B_{\nu}(T_{\text{BG}})$ at 4.67 μm . This effect can also cause the systematic trend seen in the shallow red wing in the *P*-branch. However, if $T_{\text{CO}} \sim 300 \text{ K}$, f must be very large ($\sim 10^3$) because $B_{\nu}(T_{\text{CO}})$ is at the Wien side at that wavelength. This effect would therefore appear not to fully explain the systematic trend.

We did not adopt any Doppler shifts into the modeled absorption. The implied systematic poor fit in the red wing in the *P*-branch can also be interpreted as blueshift

TABLE 4
BEST-FIT PARAMETERS AND GOODNESS OF FIT

Object	$\log N_{\text{CO}}$ (in cm^{-2})	T_{CO} (K)	v_{turb} (km s^{-1})	χ^2/dof
IRAS 06035–7102	$18.72^{+0.25}_{-0.08}$	522^{+71}_{-104}	> 49	119.5/38
IRAS 08572+3915	$19.31^{+0.09}_{-0.08}$	417^{+23}_{-23}	66^{+5}_{-4}	546.3/43
UGC 5101	$19.38^{+0.10}_{-0.09}$	506^{+35}_{-34}	65^{+5}_{-5}	747.9/49
Mrk 273	$18.27^{+0.07}_{-0.04}$	415^{+76}_{-63}	> 52	94.5/42
IRAS 19254–7245	$18.47^{+0.09}_{-0.02}$	453^{+37}_{-42}	> 62	103.0/44
IRAS 23128–5919	$19.60^{+2.61}_{-0.32}$	297^{+66}_{-169}	32^{+5}_{-11}	563.3/48
IRAS 00182–7112	$21.16^{+0.70}_{-1.06}$	329^{+124}_{-55}	28^{+7}_{-9}	133.6/30
IRAS 00397–1312	$19.48^{+0.08}_{-0.07}$	202^{+9}_{-9}	123^{+2}_{-8}	217.8/29
IRAS 00406–3127	$20.95^{+1.30}_{-1.37}$	202^{+130}_{-57}	45^{+24}_{-7}	182.7/30
IRAS 13352+6402	$19.16^{+0.23}_{-0.15}$	302^{+36}_{-40}	82^{+24}_{-16}	94.8/28

NOTE. — All errors are quoted at the 90% joint confidence level for three parameters ($\Delta\chi^2 = 6.25$), instead of for one parameter of interest. Lower limits for v_{turb} are presented if it cannot be constrained within the parameter range ($< 300 \text{ km s}^{-1}$) at the 99% joint confidence level.

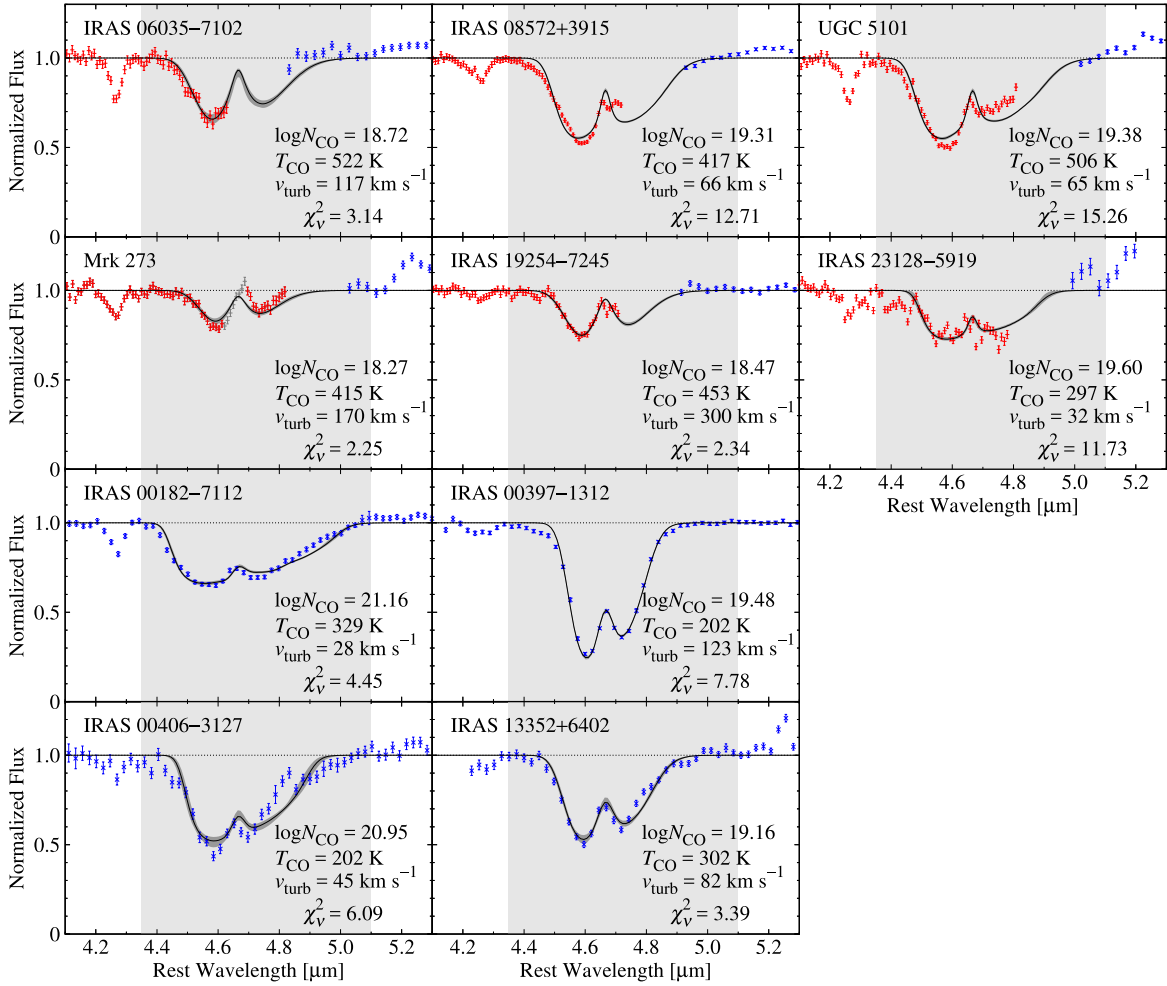


FIG. 4.— Results of gas-model fitting. Black solid lines denote the best-fit CO absorption profiles, and the accompanying gray-filled curves represent the intervals corresponding to the 90% joint confidence level. Red and blue points are data from the *AKARI*/IRC and *Spitzer*/IRS spectra, respectively. Gray shaded areas indicate the wavelength range used for the spectral fitting. Dark-gray points in the spectrum of Mrk 273 were excluded from the fitting to avoid the possible contribution from the Pfβ (4.65 μm) emission. The best-fit parameters and the goodness-of-fit $\chi^2_v \equiv \chi^2/\text{dof}$ are noted at the right bottom corners.

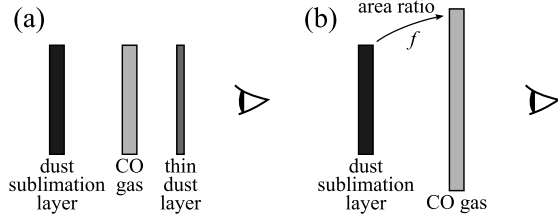


FIG. 5.— Two types of geometries beyond the model assumption. (a) Geometry in which another foreground thin dust layer is present. (b) Geometry in which the CO gas layer extends beyond the background dust sublimation layer with an area ratio f .

from the systemic velocity. A shift of $\sim 0.02 \mu\text{m}$ requires a velocity of $\sim -1000 \text{ km s}^{-1}$. Such high-velocity molecular outflows have in fact been found in far-IR OH emission lines (e.g., Fischer et al. 2010; Spoon et al. 2013) and are comparable with column densities as large as $N_{\text{H}} \sim 10^{23} \text{ cm}^{-2}$ (González-Alfonso et al. 2017). Thus, the poor fit in the P -branch may be a signature of warm molecular outflows. However, such a conclusion from only the present broad blurred absorption profiles is not robust, and verification will require other observations at higher spectral resolutions that can resolve different rotational levels.

Some other absorption bands possibly overlap the CO band. If present, ^{13}CO gas and CO ice features appear at wavelengths longer than the ^{12}CO gas band center. These would deepen the P -branch of the ^{12}CO profile, but this contribution is contrary to the observed pattern, suggesting that there is no signature of such features. On the other hand, the XCN ice feature, whose center is $4.62 \mu\text{m}$ and FWHM is $0.05 \mu\text{m}$, possibly superimposes on the R -branch of the gas phase ^{12}CO band, as was observed in the starburst/AGN galaxy NGC 4945 (Spoon et al. 2003) and the starburst galaxy NGC 253 (Yamagishi et al. 2011). However, this ice band is narrower than the observed width of the CO R -branch and thus unlikely to mimic it. Although there are weak implications of such an additional narrow absorption at the peak of the branch in some targets such as UGC 5101 (Figure 4), we cannot rule out the possibility that the responsible absorber is not XCN ice but another, colder CO gas component.

As it is difficult to discuss the above effects in detail based on the present *AKARI* and *Spitzer* spectra, we do not further pursue them in this paper.

5.2. Heating Mechanism

Our most important finding is that the observed CO gas has a high temperature and a large column density. The typical temperature $T_{\text{CO}} \sim 400 \text{ K}$ is far higher than that of molecular gas in ordinary star-forming regions ($10\text{--}10^2 \text{ K}$, Hollenbach & Tielens 1999). The typical column density $N_{\text{CO}} \sim 10^{19} \text{ cm}^{-2}$ corresponds to $N_{\text{H}_2} \sim 10^{23} \text{ cm}^{-2}$ if we assume an abundance ratio $[\text{CO}]/[\text{H}_2] = 2 \times 10^{-4}$ (Dickman 1978). Here, we consider what mechanism can heat the observed large columns of warm gas through a discussion of three candidates.

The first candidate heating source is ultraviolet (UV) photons emitted from the central accretion disk. An intense UV radiation field incident on a cloud forms a photon-dominated region (PDR) and determines its thermal and chemical structures. Several authors have

modeled the PDR under various conditions (e.g., Tielens & Hollenbach 1985; Hollenbach & Tielens 1999). Meijerink & Spaans (2005) developed PDR models at four conditions specified by the combination of the gas number density ($n_{\text{H}} = 10^3$ or $10^{5.5} \text{ cm}^{-3}$) and the incident far-UV flux ($G_0 = 10^3$ or 10^5). Here G_0 is a flux measure normalized at $1.6 \times 10^{-3} \text{ erg cm}^{-2} \text{ s}^{-1}$ (Habing 1969). In all the cases except for the high-density and low-flux case ($n_{\text{H}} = 10^{5.5} \text{ cm}^{-3}$ and $G_0 = 10^3$), the maximum gas temperature exceeds 10^3 K , which is sufficiently higher than the observed values of T_{CO} . However, in the models, the gas temperature afterward decreases steeply because of strong attenuation by dust and drops to 10^2 K before the column density N_{H} reaches 10^{22} cm^{-2} . Moreover, the CO abundance is suppressed in this PDR region due to photo-dissociation: the CO/C ratio is lower than unity at $N_{\text{H}} < 10^{22} \text{ cm}^{-2}$. The achievable warm ($> 10^2 \text{ K}$) CO column density is only $N_{\text{CO}} \sim 10^{16} \text{ cm}^{-2}$ and far smaller than the observed values ($\gtrsim 10^{18} \text{ cm}^{-2}$) by two orders of magnitude. This suggests that UV heating cannot represent the observed large columns of warm gas.

In the study of CO pure rotational emission lines, merely detecting high- J lines with a high excitation temperature does not rule out the possibility of PDRs as the origin of the emission (Mashian et al. 2015). Actually, Loenen et al. (2010) reproduced the spectral line energy distribution (SLED) of the starburst galaxy M82 up to $J = 12$ using only PDRs. However, the PDRs introduced in their analysis had column densities only on the order of $N_{\text{H}} \sim 10^{21} \text{ cm}^{-2}$. In our observation of the fundamental CO ro-vibrational transition, the broad band width was equivalent to the detection of highly excited lines at $J \gtrsim 20$. More importantly, the obtained column density is too large ($N_{\text{H}} \gtrsim 10^{22} \text{ cm}^{-2}$) to be reproduced by PDRs and requires other heating sources.

The next candidate is shock heating. Given that many of the observed galaxies are merging systems or in disturbed morphologies, it is reasonable to conjecture that their gas is powered by shocks arising from turbulent motion. A number of studies have discussed the physical and chemical processes in shock propagation in interstellar clouds (e.g., McKee et al. 1984; Hollenbach & McKee 1989; Neufeld & Dalgarno 1989). With a shock velocity of $\sim 100 \text{ km s}^{-1}$ and a pre-shock density of $10^4\text{--}10^6 \text{ cm}^{-3}$, the post-shock temperature structure begins with the initial value of $\gtrsim 10^4 \text{ K}$, where the gas is heated by UV photons from the vicinity of the shock front. The temperature then gradually decreases until the UV radiation is sufficiently attenuated and molecular recombination becomes effective. After this point, OH molecules become the major coolant and the gas temperature rapidly falls below $\sim 10^3 \text{ K}$. This rapid drop is followed by an equilibrium between OH cooling and heating owing to H_2 formation on dust grains. CO rotational transitions also significantly contribute to cooling in this phase. Under this balance, the temperature remains at $\sim 10^2 \text{ K}$ until H_2 formation is completed.

Because the molecular-forming region downstream of a shock provides gas temperatures higher than 10^2 K , shock heating can explain observed T_{CO} values. On the other hand, the scale of the column density in the warm gas layer is $N_{\text{H}} \lesssim 10^{22} \text{ cm}^{-2}$ and the CO relative abun-

dance is nearly constant at $\sim 10^{-4}$ (Hollenbach & McKee 1989; Neufeld & Dalgarno 1989). Hence, shock heating can produce a warm CO gas with column densities of up to $N_{\text{CO}} \sim 10^{18} \text{ cm}^{-2}$. This upper bound is comparable to the smallest N_{CO} we observed. Thus, while there is still room for a partial contribution from shock heating, it cannot fully account for the heating mechanism of the CO gas.

The third heating source candidate is X-ray photons emitted from the nuclear region of the AGN. A strong X-ray radiation field incident on a cloud creates an X-ray-dominated region (XDR) that drives its internal thermal and chemical processes. Although this process is similar to PDR formation by UV photons, X-ray photons can penetrate more deeply into clouds because of their small cross sections. Meijerink & Spaans (2005) modeled XDRs with chemical reactions under four conditions involving combinations of two densities ($n_{\text{H}} = 10^3$ and $10^{5.5} \text{ cm}^{-3}$) and two incident X-ray fluxes ($F_{\text{X}} = 1.6$ and $160 \text{ erg cm}^{-2} \text{ s}^{-1}$). In all cases except those with high density and low flux, the simulated temperatures are in the range 10^2 – 10^4 K and accord with observed T_{CO} values. Moreover, the temperatures remain higher than 10^2 K up to a column density of $N_{\text{H}} \sim 10^{24} \text{ cm}^{-2}$. This scale of heating is more than two orders of magnitude larger than those resulting from the previous two mechanisms. In all cases, N_{CO} reaches 10^{18} cm^{-2} before the temperature fall to 10^2 K (compare Figures 6 and 8 in Meijerink & Spaans 2005), demonstrating that such XDRs can account for the observed warm CO gas of a large column density. In addition, the dense and intense case ($n_{\text{H}} = 10^{5.5} \text{ cm}^{-3}$ and $F_{\text{X}} = 160 \text{ erg cm}^{-2} \text{ s}^{-1}$) gives the largest N_{CO} at $T = 100 \text{ K}$ among all cases (10^{20} cm^{-2}), suggesting that the two sources of large $N_{\text{CO}} \sim 10^{21} \text{ cm}^{-2}$, IRAS 00182–7112 and IRAS 00406–3127, require more extreme XDRs.

We attempted to distinguish shock and X-ray heating on the basis of the CO SLED of the rotational transitions. Such lines are one of the major coolants in a shocked gas. This discussion is analogous to that argued by Meijerink et al. (2013) for NGC 6240 and Mrk 231, which are nearby merger/starburst and Sy1 galaxies, respectively. These two galaxies are similar in terms of their CO SLED shapes, with a flat distribution up to higher rotational levels, but differ in terms of their line-to-continuum ratios $L_{\text{CO}}/L_{\text{IR}}$, where L_{CO} is the total luminosity of the ^{12}CO lines including CO $J = 1$ –0 through $J = 13$ –12. While the ratio in Mrk 231 is $\sim 6 \times 10^{-5}$ (van der Werf et al. 2010), that in NGC 6240 is $\sim 7 \times 10^{-4}$, which is approximately an order of magnitude higher than the former value (Meijerink et al. 2013). The authors concluded that this large difference results from the difference in gas heating processes in the two galaxies. UV and X-ray photons effectively heat both gas and dust, and resulting in a far-IR spectrum that is continuum-dominated and, consequently, a small line-to-continuum ratio. The authors also predicted the maximum line-to-continuum ratio in PDRs and XDRs as $\sim 10^{-4}$. Shocks, on the other hand, selectively heat gas by compression, maintaining the thermal decoupling of dust and attaining ratios higher than 10^{-4} . This leads to the conclusion that the dominant power sources for the CO gas clouds emitting rotational lines in Mrk 231 and NGC 6240 are

UV to X-ray photons and shocks, respectively.

To make a similar analysis, we referred to Pearson et al. (2016), who observed the CO emission lines from $J = 5$ –4 to $J = 13$ –12 in 43 ULIRGs using the *Herschel Space Observatory*. Seven of their sample galaxies are included in our targets, namely, all of the *AKARI* targets and IRAS 00397–1312. We calculated the sub-total CO luminosity L'_{CO} spanning from $J = 5$ –4 to $J = 13$ –12 in the seven objects and then evaluated the line-to-continuum ratio from $L'_{\text{CO}}/L_{\text{IR}}$. We also derived the ratios in NGC 6240² and Mrk 231 for comparison and found the values of 4×10^{-4} and 6×10^{-5} , respectively. Among the seven galaxies in our sample, the lowest ratio was found in IRAS 08572+3915, in which the ratio is 3×10^{-5} , which is even smaller than that in Mrk 231. This object also shows a continuum dominated spectrum in the near- and mid-IR region. These facts strongly rule out the possibility of powerful shock heating within the galaxy. On the other hand, the highest ratio was found in IRAS 06035–7102, where the ratio is 2×10^{-4} , suggesting the possibility of shock heating, a conclusion supported by the facts that: a) the N_{CO} value found in this galaxy is relatively smaller than that in the other targets, and b): a widely used shock tracer H_2 vibrational emission around $2 \mu\text{m}$ was detected in this source (Dannerbauer et al. 2005). However, as the ratio $L'_{\text{CO}}/L_{\text{IR}}$ is lower by a factor of two than that in NGC 6240, shocks in IRAS 06035–7102 would not be as energetic as those in NGC 6240. In the remaining four galaxies, the ratio ranged within $(0.8\text{--}1.0) \times 10^{-4}$, and there was no evidence of shock heating in these objects.

Given the above discussion, we conclude that the most reasonable heating mechanism of observed warm CO gas with large column densities is X-ray heating, which leads to the further conclusion that the observed CO gas is in the vicinity of the nucleus. Although the possibility that shock heating accounts for a substantial fraction of the total power cannot be ruled out in some objects, its contribution must be smaller than that of X-ray photons. In the following discussion, we presuppose that the primal heating source of the CO gas observed in absorption is X-ray photons from the central region of the AGN.

5.3. The Relations between the Column Density, Temperature, and IR Luminosity

Figure 6 plots T_{CO} versus N_{CO} , showing that T_{CO} decreases with N_{CO} . Although the confidence ranges of the best-fits show a strong degeneracy between the two parameters, these ranges are smaller than the scale of the overall decreasing tendency. This result can be interpreted as an attenuation in which the gas a large-column distant from the heating source is heated less than gas near the source in a small column if the heating powers in the respective targets are nearly the same. Figure 7 shows that the dependence of N_{CO} and T_{CO} on the IR luminosity, L_{IR} , is not clear. This supports the interpretation that the heating process in the CO gas observed in absorption is a local phenomenon occurring near the

² Note that the line luminosities in NGC 6240 measured by Pearson et al. (2016) were substantially lower than the measurements by Meijerink et al. (2013). Pearson et al. (2016) claimed that the reason for this is unclear, as the two papers had used the same observation.

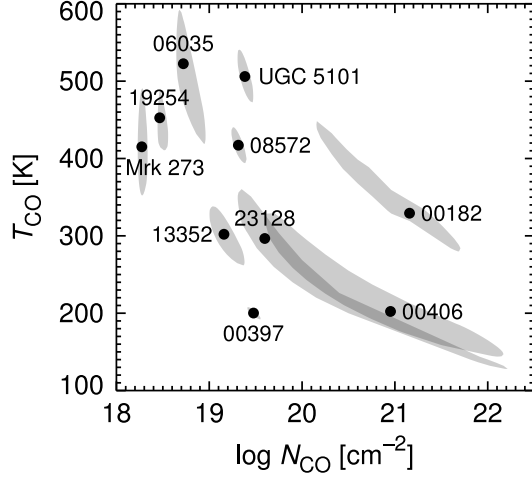


FIG. 6.— Plot of T_{CO} versus N_{CO} . Black points indicate the best-fit values. Gray shaded areas are the projection of the three-dimensional 90% joint confidence regions along the v_{turb} axis. The unprojected 3D confidence regions are shown in Figure 12.

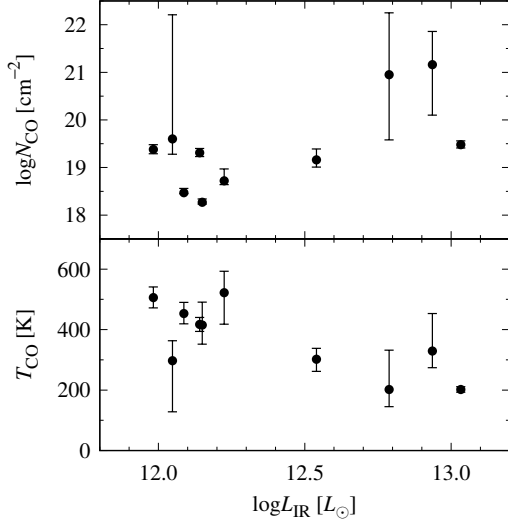


FIG. 7.— Dependence of N_{CO} (top) and T_{CO} (bottom) on L_{IR} . The abscissa is the logarithm of L_{IR} in units of the solar luminosity L_{\odot} .

power source and is not tightly related to the global activities of the host galaxy.

5.4. Comparison with X-Ray Observations

To clarify the location of the region in which CO absorption originates, we compared the obtained CO column densities with neutral column densities estimated from other X-ray observations. Brightman & Nandra (2011) performed a systematic X-ray spectral analysis for the *XMM-Newton* data (0.2–10 keV) of 126 nearby galaxies and investigated their AGN properties using a spectral model that assumes a spherical toroidal obscuring material. Four objects in their sample are common with our targets. Table 5 summarizes their line-of-sight hydrogen column densities determined by the X-ray spectral analysis.

We converted N_{CO} into N_{H} assuming a ratio of $N_{\text{CO}}/N_{\text{H}} \sim 10^{-4}$ for the XDRs in the high-density cases

TABLE 5
COLUMN DENSITY INFERRED FROM
X-RAY OBSERVATIONS

Object	$N_{\text{H,X}}$ (10^{22} cm^{-2})
UGC 5101	$49.6^{+25.4}_{-18.2}$
Mrk 273	$59.7^{+17.1}_{-12.8}$
IRAS 19254–7245	$38.1^{+39.2}_{-21.7}$
IRAS 23128–5919	> 150

NOTE. — Column 1: object name. Column 2: hydrogen absorption column density, with errors quoted at 90% confidence level for one parameter of interest (Brightman & Nandra 2011).

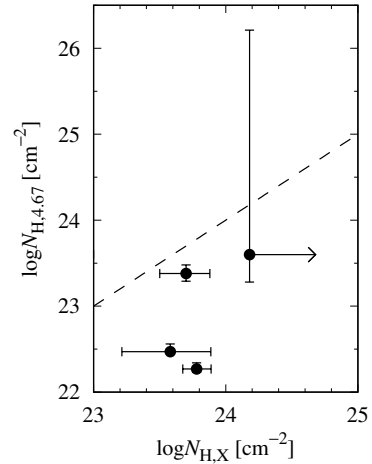


FIG. 8.— Comparison of the hydrogen column densities derived from an X-ray spectral analysis (abscissa; Table 5) and from CO absorption (ordinate). The dashed line denotes the identity.

of Meijerink & Spaans (2005). Note that $N_{\text{CO}}/N_{\text{H}}$ is not constant if the incident X-ray field is intense, as the CO abundance is suppressed at small N_{H} ; here, we ignore this dependence for simplicity. Figure 8 compares the two types of hydrogen column density. The hydrogen column density derived from the CO absorption, $N_{\text{H},4.67}$, is 2–30 times smaller than that inferred from the X-ray spectral analysis, $N_{\text{H,X}}$. This comparison indicates that the two columns trace the amount of gas at different depths. The X-ray-derived column density $N_{\text{H,X}}$ measures the gas in front of the central AGN nucleus using the X-ray radiation from it as the background. By contrast, $N_{\text{H},4.67}$ should measure the gas outside the X-ray emitting region, tracing a smaller amount of foreground gas. This consideration is consistent with the assumption that the near-IR background continuum source for CO absorption is a region in front of the nucleus being warmed by the radiation from the nucleus. Therefore, we conclude that the CO absorption originates in molecular gas distributed outside the X-ray emitting region.

5.5. Comparison with the 9.7 μm Silicate Absorption

Another major indicator of the degree of obscuration is the strength of the 9.7 μm silicate dust feature, as is seen in Figures 1 and 2. The optical depth of the feature $\tau_{9.7}$

TABLE 6
9.7 μm SILICATE FEATURE FROM LITERATURE

Object	$\tau_{9.7}$	$N_{\text{H},9.7}$ (10^{22} cm^{-2})
IRAS 06035–7102	2.9 (10%) ^a	9.9
IRAS 08572+3915	3.8 (5%) ^b	13
UGC 5101	1.9 (10%) ^a	6.5
Mrk 273	2.3 (10%) ^a	7.9
IRAS 19254–7245	1.5 (10%) ^a	5.1
IRAS 00182–7112	3.1 (10%) ^a	11
IRAS 00397–1312	2.7 (5%) ^c	9.2
IRAS 00406–3127	2.0 (10%) ^a	6.8

NOTE. — Column 1: object name. Column 2: optical depth of the 9.7 μm silicate dust absorption with uncertainty in parenthesis. Column 3: hydrogen column density calculated from $\tau_{9.7}$ (see the text).

^a Dartois & Muñoz-Caro (2007).

^b Imanishi et al. (2007).

^c Imanishi (2009).

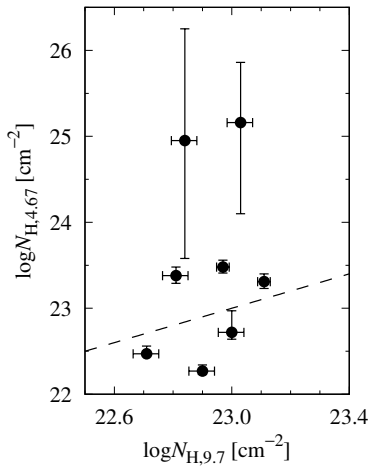


FIG. 9.— Comparison of hydrogen column densities derived from the 9.7 μm silicate dust absorption strength (abscissa; Table 6) and from the CO absorption (ordinate). The dashed line denotes the identity.

in nearby AGNs have been measured in several studies (e.g., Dartois & Muñoz-Caro 2007; Imanishi et al. 2007; Imanishi 2009). The depth $\tau_{9.7}$ can be converted into the hydrogen column density using two relations connected to visual extinction A_V : $A_V/\tau_{9.7} = 18.0 \text{ mag}$ (Whittet 2003), and $N_{\text{H}}/A_V = 1.9 \times 10^{21} \text{ cm}^{-2} \text{ mag}^{-1}$ (Bohlin et al. 1978). Table 6 cites the values of $\tau_{9.7}$ from other papers and tabulates the derived column density, $N_{\text{H},9.7}$. Figure 9 compares the two types of hydrogen column density, $N_{\text{H},4.67}$ and $N_{\text{H},9.7}$. In contrast to the comparison with the X-ray observations, $N_{\text{H},4.67}$ is similar to or a bit larger than $N_{\text{H},9.7}$. We conclude that CO-absorbing gas and silicate dust roughly coexist in the same region.

5.6. Distribution of the CO Gas

In our model, we assume that the covering factor of CO gas is unity. This assumption is not trivial but strongly supported by the observed deep absorption profiles. Such absorption indicates that the continuum source is almost entirely covered by the foreground gas. Because molecular clouds in star-forming regions distribute randomly,

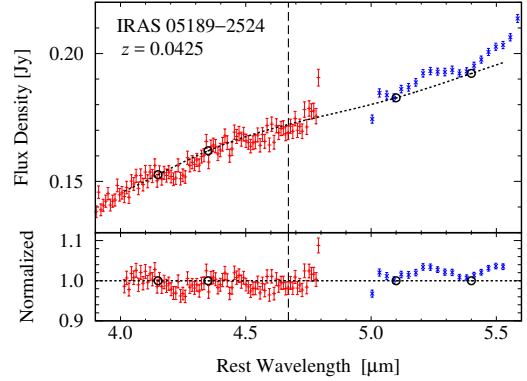


FIG. 10.— Top: 4.0–5.5 μm spectrum of the Sy2 galaxy IRAS 05189–2524. Red and blue points represent the *AKARI* and *Spitzer* data, observation ID 1100129.1 and AOR key 16909568, respectively. Data reduction was performed in the manner described in Section 2. The black dotted line denotes the continuum curve determined as explained in Section 3.1. The black dashed line indicates the expected wavelength of the CO band center. Bottom: continuum-normalized spectrum of the same galaxy.

they cannot explain a large covering factor close to unity. Thus, we assume that the absorber is a molecular cloud just in front of the continuum source.

It is remarkable that a significant fraction of Sy2 galaxies do not show CO absorption. In the *AKARI* program AGNUL, IRAS 05189–2524, which is classified as Sy2 or hidden broad-line Sy1 (Véron-Cetty & Véron 2006), does not show any signature of CO absorption, as shown in Figure 10. Lutz et al. (2004) searched *ISO* spectra of nearby 19 type-1 and 12 type-2 AGNs for CO absorption, but none showed the signature of the absorption. One of their targets, the famous Sy2 galaxy NGC 1068, was re-observed by Geballe et al. (2009) using UKIRT, with CO absorption once again undetected. Given the implications of the comparison with X-ray observations, the CO absorption is likely to trace the region outside the X-ray emitting region. The close-to-unity covering factor suggests that the CO absorption originates near the dust sublimation layer at the inner rim of the obscuring material surrounding the nucleus. Here we speculate that the presence or absence of CO absorption originates from a complex innermost geometry in the putative AGN torus, e.g., a concave dust sublimation layer arising from an anisotropic radiation from the accretion disk (Kawaguchi & Mori 2010, 2011) or a turbulent structure near the nucleus arising from the interaction with other galaxies.

6. CONCLUSION

In this paper, we present a systematic spectral analysis of the CO ro-vibrational absorption band (4.67 μm) toward ten nearby obscured AGNs observed with the *AKARI* and *Spitzer* space telescopes. Using a gas model assuming LTE, slab geometry, and a single component gas, the CO column density and gas temperature were estimated for each target. The average CO column density of the sample was found to be $N_{\text{CO}} \sim 10^{19.5} \text{ cm}^{-2}$, which corresponds to a hydrogen column density of $N_{\text{H}} \sim 10^{23.5} \text{ cm}^{-2}$ if we assume a standard abundance ratio $[\text{CO}]/[\text{H}] \sim 10^{-4}$. This large column density indicates that the AGNs are heavily obscured. On the other hand, the average temperature was found to be 360 K, which

is much higher than the typical value in normal star-forming regions.

The observed warm gas of a large column density cannot be represented by UV heating or shock heating. The former can heat gas up to 10^3 K, but its maximum heating depth is only $N_{\text{CO}} \sim 10^{16} \text{ cm}^{-2}$, which is two orders of magnitude smaller than the observed values. The latter can make gas warm ($\sim 10^2$ K) up to $N_{\text{CO}} \sim 10^{18} \text{ cm}^{-2}$, a column density comparable to the smallest N_{CO} we observed. However, the low line-to-continuum ratios in the far-IR region of our sample galaxies indicate that, in addition to gas, dust is also heated up. This does not occur under shock heating, in which gas and dust are thermally decoupled. We conclude that the most convincing heating source is X-ray photons emitted from the nucleus. This mechanism can heat gas up to even $N_{\text{CO}} \sim 10^{20} \text{ cm}^{-2}$, which is large enough to account for the observed values over 10^2 K. This conclusion suggests that the region probed by the CO absorption should be in the vicinity of the nucleus.

A comparison with an X-ray spectral analysis (Brightman & Nandra 2011) shows that the hydrogen column density derived from conversion from the CO column density is 2–30 times smaller than that inferred from the X-ray analysis. We conclude that the region probed by the near-IR CO absorption is located outside the X-ray emitting region. Moreover, the close-to-unity covering factor of the CO gas suggested by the observed deep absorption indicates that the gas is close to the continuum source, which we hypothesize to be the dust sublimation layer at the inner rim of the obscuring material around the AGN. In contrast to the comparison with the X-ray observations, the hydrogen column density derived from CO absorption is similar to or a bit larger than that calculated from the optical depth of the $9.7 \mu\text{m}$ silicate dust absorption. We conclude that CO-absorbing gas and silicate dust roughly coexist in the same region.

We reconfirmed a previously remarked-upon fact that not all Sy2 galaxies show CO absorption (Lutz et al. 2004; Geballe et al. 2009). The cryogenic phase *AKARI* AGNUL results for the Sy2 galaxy IRAS 05189–2524 do not show any signature of the feature. We speculate that the presence or absence of this absorption reflects the complex innermost geometry of the putative AGN torus, e.g., as a concave dust sublimation layer generated by anisotropic radiation from the accretion disk (Kawaguchi & Mori 2010, 2011) or a turbulent structure near the nucleus caused by interaction with other galaxies.

The authors thank the anonymous referee for careful review and helpful suggestions. The authors are grateful to H. Spoon and J. Cami for providing us with detailed information on their analysis of IRAS 00182–7112 together with insightful comments, and to F. Usui for supporting us in the data reduction of the *AKARI* spectroscopy. This work is supported by Grant-in-Aid for JSPS Research Fellows Grant Number JP17J01789 (S.B.) and for Scientific Research Grant Number JP26247030 (T.N.).

This research is based on observations with *AKARI*, a JAXA project with the participation of ESA. This work is based on observations made with the *Spitzer Space Telescope*, obtained from the NASA/IPAC Infrared Science Archive, both of which are operated by the Jet Propulsion Laboratory, California Institute of Technology under a contract with the National Aeronautics and Space Administration. This publication makes use of data products from the *Wide-field Infrared Survey Explorer*, which is a joint project of the University of California, Los Angeles, and the Jet Propulsion Laboratory/California Institute of Technology, and *NEOWISE*, which is a project of the Jet Propulsion Laboratory/California Institute of Technology. *WISE* and *NEOWISE* are funded by the National Aeronautics and Space Administration.

REFERENCES

- Allen, D. A., Norris, R. P., Meadows, V. S., & Roche, P. F. 1991, *MNRAS*, 248, 528
- Antonucci, R. 1993, *ARA&A*, 31, 473
- Armus, L., Heckman, T. M., & Miley, G. K. 1989, *ApJ*, 347, 727
- Baba, S., Nakagawa, T., Shirahata, M., et al. 2016, *PASJ*, 68, 27
- Barvainis, R. 1987, *ApJ*, 320, 537
- Black, J. H., van Dishoeck, E. F., Willner, S. P., & Woods, R. C. 1990, *ApJ*, 358, 459
- Bohlin, R. C., Savage, B. D., & Drake, J. F. 1978, *ApJ*, 224, 132
- Braito, V., Reeves, J. N., Della Ceca, R., et al. 2009, *A&A*, 504, 53
- Brightman, M., & Nandra, K. 2011, *MNRAS*, 413, 1206
- Cami, J. 2002, PhD thesis, University of Amsterdam
- Dannerbauer, H., Rigopoulou, D., Lutz, D., et al. 2005, *A&A*, 441, 999
- Dartois, E., & Muñoz-Caro, G. M. 2007, *A&A*, 476, 1235
- Dickman, R. L. 1978, *ApJS*, 37, 407
- Draine, B. T. 2003, *ARA&A*, 41, 241
- Duc, P.-A., Mirabel, I. F., & Maza, J. 1997, *A&AS*, 124, doi:10.1051/aas:1997205
- Fischer, J., Sturm, E., González-Alfonso, E., et al. 2010, *A&A*, 518, L41
- Frerking, M. A., Langer, W. D., & Wilson, R. W. 1982, *ApJ*, 262, 590
- García-Burillo, S., Combes, F., Ramos Almeida, C., et al. 2016, *ApJ*, 823, L12
- Geballe, T. R., Goto, M., Usuda, T., Oka, T., & McCall, B. J. 2006, *ApJ*, 644, 907
- Geballe, T. R., Mason, R. E., Rodríguez-Ardila, A., & Axon, D. J. 2009, *ApJ*, 701, 1710
- González-Alfonso, E., Fischer, J., Spoon, H. W. W., et al. 2017, *ApJ*, 836, 11
- Habing, H. J. 1969, *Bull. Astron. Inst. Netherlands*, 20, 177
- Hollenbach, D., & McKee, C. F. 1989, *ApJ*, 342, 306
- Hollenbach, D. J., & Tielens, A. G. G. M. 1999, *Reviews of Modern Physics*, 71, 173
- Houck, J. R., Roellig, T. L., van Cleve, J., et al. 2004, *ApJS*, 154, 18
- Imanishi, M. 2009, *ApJ*, 694, 751
- Imanishi, M., Dudley, C. C., Maiolino, R., et al. 2007, *ApJS*, 171, 72
- Imanishi, M., Nakagawa, T., Ohya, Y., et al. 2008, *PASJ*, 60, 489
- Imanishi, M., Nakagawa, T., Shirahata, M., Ohya, Y., & Onaka, T. 2010, *ApJ*, 721, 1233
- IRS Instrument Team and Science User Support Team. 2011, *IRS Instrument Handbook*, 5th edn., IRS Instrument Team and Science User Support Team
- Iwasawa, K., Sanders, D. B., Teng, S. H., et al. 2011, *A&A*, 529, A106
- Jarrett, T. H., Cohen, M., Masci, F., et al. 2011, *ApJ*, 735, 112
- Kawaguchi, T., & Mori, M. 2010, *ApJ*, 724, L183
- . 2011, *ApJ*, 737, 105
- Kim, D.-C., & Sanders, D. B. 1998, *ApJS*, 119, 41
- Lacy, J. H., Knacke, R., Geballe, T. R., & Tokunaga, A. T. 1994, *ApJ*, 428, L69
- Lahuis, F., Spoon, H. W. W., Tielens, A. G. G. M., et al. 2007, *ApJ*, 659, 296
- Loenen, A. F., van der Werf, P. P., Güsten, R., et al. 2010, *A&A*, 521, L2
- Lutz, D., Sturm, E., Genzel, R., et al. 2000, *ApJ*, 536, 697

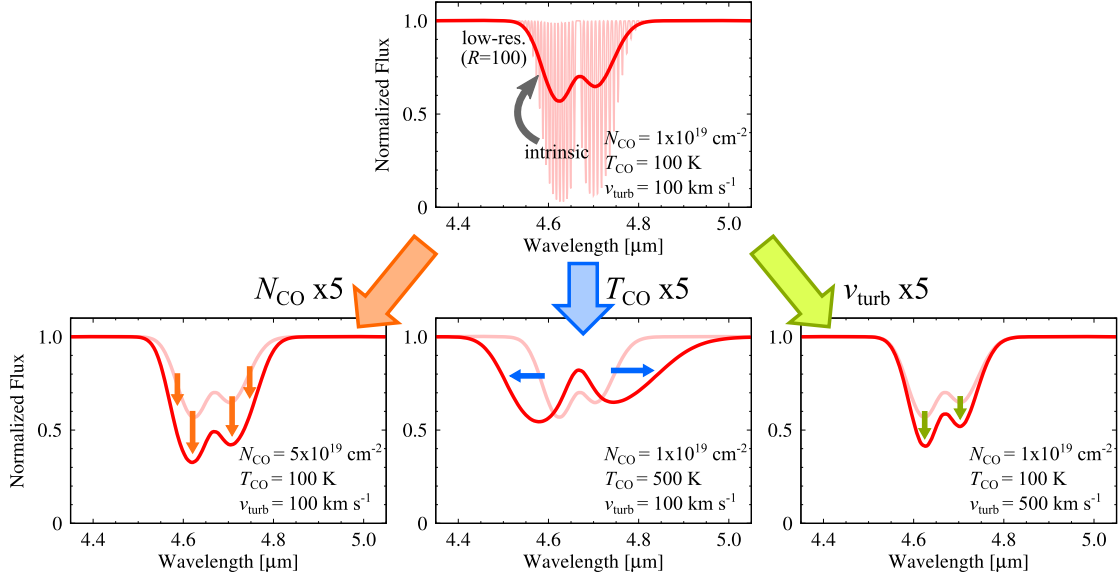


FIG. 11.— Parameter dependence of the CO absorption model. The top panel compares the intrinsic model spectrum for the parameters noted at the right bottom corner with a blurred spectrum for a low spectral resolution ($R = 100$). The bottom panels illustrate the changes in the absorption profile from the top panel when one parameter is multiplied by a factor of five.

- Lutz, D., Sturm, E., Genzel, R., Spoon, H. W. W., & Stacey, G. J. 2004, *A&A*, 426, L5
- Lutz, D., Feuchtgruber, H., Genzel, R., et al. 1996, *A&A*, 315, L269
- Mashian, N., Sturm, E., Sternberg, A., et al. 2015, *ApJ*, 802, 81
- McKee, C. F., Chernoff, D. F., & Hollenbach, D. J. 1984, in *Astrophysics and Space Science Library*, Vol. 108, Galactic and Extragalactic Infrared Spectroscopy, ed. M. F. Kessler & J. P. Phillips, 103–131
- Meijerink, R., & Spaans, M. 2005, *A&A*, 436, 397
- Meijerink, R., Kristensen, L. E., Weiß, A., et al. 2013, *ApJ*, 762, L16
- Murakami, H., Baba, H., Barthel, P., et al. 2007, *PASJ*, 59, 369
- Nandra, K., & Iwasawa, K. 2007, *MNRAS*, 382, L1
- Nardini, E., & Risaliti, G. 2011, *MNRAS*, 415, 619
- Neufeld, D. A., & Dalgarno, A. 1989, *ApJ*, 340, 869
- Ohya, Y., Onaka, T., Matsuhara, H., et al. 2007, *PASJ*, 59, 411
- Onaka, T., Matsuhara, H., Wada, T., et al. 2007, *PASJ*, 59, 401
- Pearson, C., Rigopoulou, D., Hurley, P., et al. 2016, *ApJS*, 227, 9
- Sanders, D. B., Mazzarella, J. M., Kim, D.-C., Surace, J. A., & Soifer, B. T. 2003, *AJ*, 126, 1607
- Sanders, D. B., & Mirabel, I. F. 1996, *ARA&A*, 34, 749
- Sargsyan, L., Weedman, D., Lebouteiller, V., et al. 2011, *ApJ*, 730, 19
- Saunders, W., Sutherland, W. J., Maddox, S. J., et al. 2000, *MNRAS*, 317, 55
- Scoville, N. Z., Evans, A. S., Thompson, R., et al. 2000, *AJ*, 119, 991
- Shirahata, M., Nakagawa, T., Usuda, T., et al. 2013, *PASJ*, 65, 5
- Smith, J. D. T., Draine, B. T., Dale, D. A., et al. 2007, *ApJ*, 656, 770
- Soifer, B. T., Neugebauer, G., Matthews, K., et al. 2000, *AJ*, 119, 509
- Spoon, H. W. W., Keane, J. V., Cami, J., et al. 2005, in *IAU Symposium*, Vol. 231, *Astrochemistry: Recent Successes and Current Challenges*, ed. D. C. Lis, G. A. Blake, & E. Herbst, 281–290
- Spoon, H. W. W., Moorwood, A. F. M., Pontoppidan, K. M., et al. 2003, *A&A*, 402, 499
- Spoon, H. W. W., Armus, L., Cami, J., et al. 2004, *ApJS*, 154, 184
- Spoon, H. W. W., Farrah, D., Lebouteiller, V., et al. 2013, *ApJ*, 775, 127
- Storey, P. J., & Hummer, D. G. 1995, *MNRAS*, 272, 41, link from ADS to On-line Data
- Sturm, E., Lutz, D., Verma, A., et al. 2002, *A&A*, 393, 821
- Tielens, A. G. G. M., & Hollenbach, D. 1985, *ApJ*, 291, 722
- van der Werf, P. P., Isaak, K. G., Meijerink, R., et al. 2010, *A&A*, 518, L42
- Veilleux, S., Kim, D.-C., & Sanders, D. B. 1999, *ApJ*, 522, 113
- Veilleux, S., Kim, D.-C., Sanders, D. B., Mazzarella, J. M., & Soifer, B. T. 1995, *ApJS*, 98, 171
- Véron-Cetty, M.-P., & Véron, P. 2006, *A&A*, 455, 773
- Watson, D. M., Genzel, R., Townes, C. H., & Storey, J. W. V. 1985, *ApJ*, 298, 316
- Werner, M. W., Roellig, T. L., Low, F. J., et al. 2004, *ApJS*, 154, 1
- Whittet, D. C. B., ed. 2003, *Dust in the galactic environment*
- Wright, E. L., Eisenhardt, P. R. M., Mainzer, A. K., et al. 2010, *AJ*, 140, 1868
- Yamagishi, M., Kaneda, H., Ishihara, D., et al. 2011, *ApJ*, 731, L20

APPENDIX

PARAMETER DEPENDENCE OF THE ABSORPTION PROFILE

Figure 11 describes how our model depends on three parameters. If the column density, N_{CO} , increases, the absorption profile becomes deeper because the optical depth is proportional to N_{CO} . If the temperature, T_{CO} , increases, the profile becomes wider because higher rotational levels are populated. If the velocity width, v_{turb} , increases, the profile becomes deeper at the peaks of the P - and R -branches because the equivalent width is broadened only when the absorption is saturated. When the absorption is weak, we cannot determine v_{turb} from the model fitting unless we resolve rotational levels with a high spectral resolution. In this paper, however, we do not face this problem in most of the targets because they show sufficiently deep absorption profiles. We restrict the range of v_{turb} to less than 300 km s^{-1} because values higher than this upper limit do not substantially affect the profile as they involve two neighboring rotational lines to completely blend with each other.

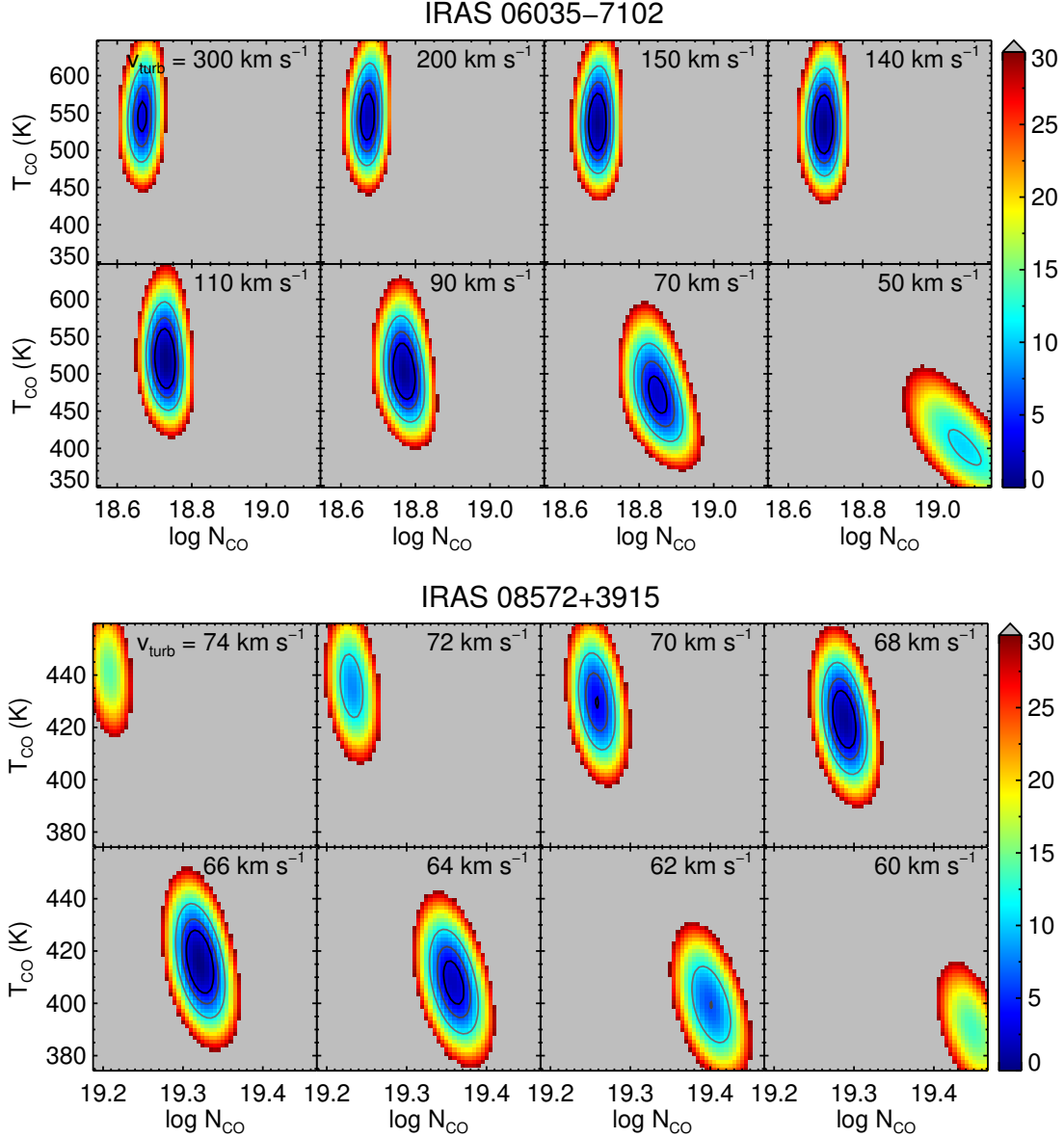


FIG. 12.— Color maps of the $\Delta\chi^2$ values of the best-fit models shown in Figure 4 whose parameters are tabulated in Table 4. Each panel shows a slice of the three-dimensional parameter space at the turbulent velocity v_{turb} noted at the top right corner. From inside to outside, the closed solid curves denote the 68%, 90%, and 99% joint confidence levels, respectively.

$\Delta\chi^2$ MAP

Figure 12 shows a set of color maps of the $\Delta\chi^2$ value for all of the targets. The maps clearly show the degeneracy among the parameters. Large values of N_{CO} anti-correlates with T_{CO} and v_{turb} . The N_{CO} versus T_{CO} anti-correlation can be interpreted as follows. At large N_{CO} , the absorption is nearly saturated. Because the depths at the two peaks of the absorption profile do not change significantly with N_{CO} , the depths at the band wings become more important in the determination of the solution. However, high values of T_{CO} instead of N_{CO} can also deepen the band wings, which results in the anti-correlation between N_{CO} and T_{CO} . On the other hand, the N_{CO} versus v_{turb} anti-correlation originates because the two parameters similarly deepen the band profile when the absorption is saturated.

COMPARISONS WITH PREVIOUS CO ANALYSES

IRAS 00182-7112

Our best-fit model for IRAS 00182-7112 (or IRAS F00183-7111) had a large column density and did not coincide with that of S04, who had performed a similar gas model fitting for a *Spitzer*/IRS spectrum based on an earlier IRS calibration. Our best-fitting parameters were, as tabulated in Table 3, $N_{\text{CO}} = 10^{21.2}$ cm⁻², $T_{\text{CO}} = 329$ K, and $v_{\text{turb}} = 28$ km s⁻¹, whereas those found by S04 were $10^{19.5}$ cm⁻², 720 K, and 50 km s⁻¹. The 99% joint confidence

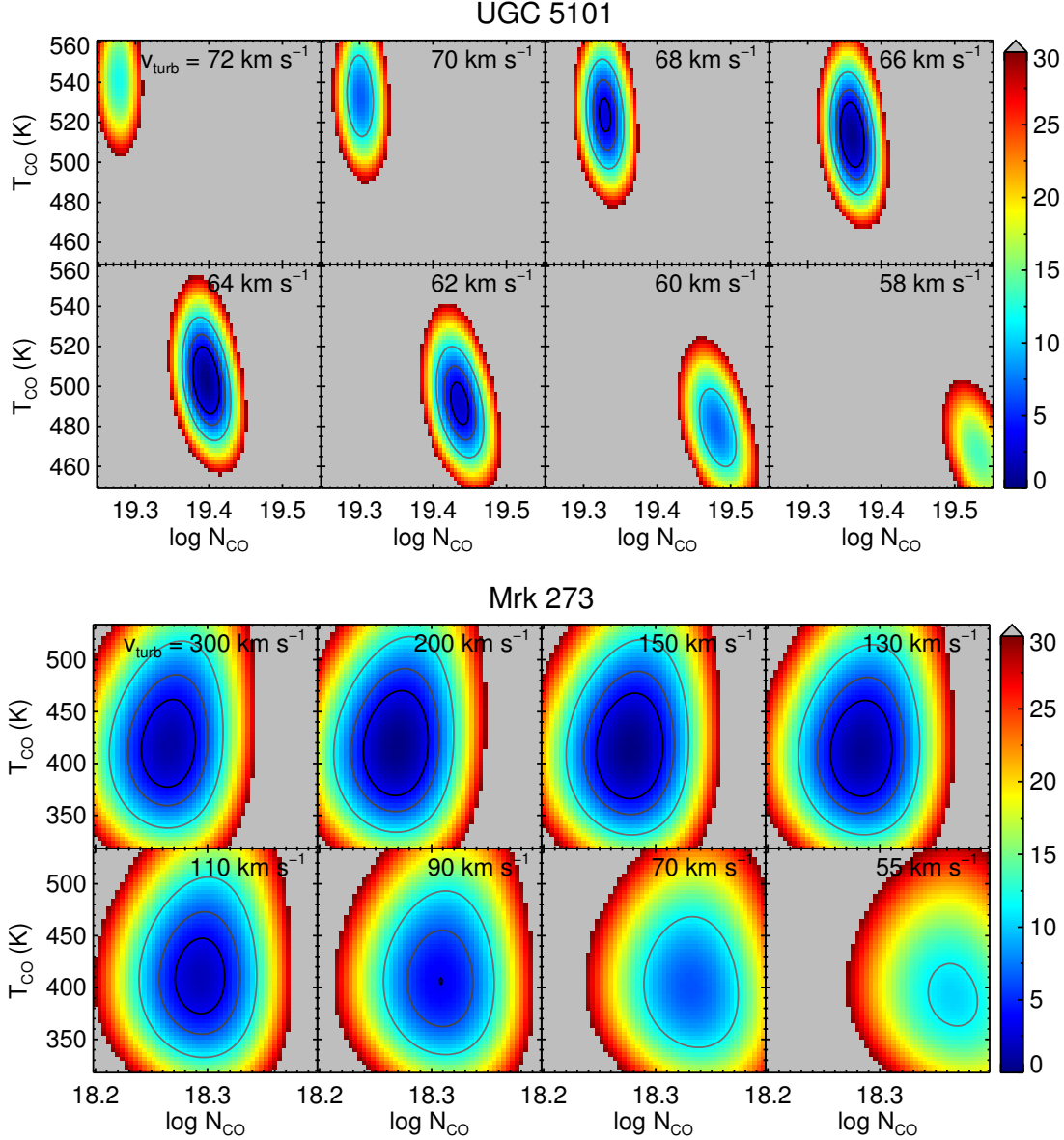


FIG. 12.— (Continued)

region of our best-fit did not include the solution of S04. However, in the analysis of S04, another solution with $N_{\text{CO}} = 10^{21.5} \text{ cm}^{-2}$, $T_{\text{CO}} = 400 \text{ K}$, and $v_{\text{turb}} = 25 \text{ km s}^{-1}$, which is similar to our result, was also found (H. Spoon & J. Cami, private communication). We therefore finally adopted our obtained large-column solution even though this solution has an uncertainty in the amount of gas hidden behind the $\tau = 1$ surface.

IRAS 08572+3915

IRAS 08572+3915 comprises two nuclei, with the one in the northwest (NW) being brighter than the one in southeast (SE) by 2.2 magnitudes at $2.2 \mu\text{m}$ (Scoville et al. 2000). The CO ro-vibrational absorption lines in IRAS 08572+3915 NW were first detected by Geballe et al. (2006) using UKIRT, and then observed with higher quality by S13 using Subaru. S13 obtained a high spectral resolution spectrum ($R \sim 5000$, $\Delta v \sim 60 \text{ km s}^{-1}$) with individual absorption lines resolved and revealed a velocity profile comprising three distinct components centered at 0, -160 , and $+100 \text{ km s}^{-1}$ relative to the systemic velocity of the galaxy. The authors analyzed the spectrum under the assumption of a three-component gas. Note that the numbers below are quoted from the full coverage case of S13, which is equivalent to our assumption, although the authors also discussed a partial coverage case. The first component was the blueshifted component, which had the largest CO column density of $2.7 \times 10^{18} \text{ cm}^{-2}$, a warm temperature of 325 K , and a velocity width broader than 200 km s^{-1} . The second component was at the systemic velocity, with a column density of $5.7 \times 10^{17} \text{ cm}^{-2}$ and a temperature of 23 K . The third was the redshifted component, which was weaker than the other two components ($\sim 10^{17} \text{ cm}^{-2}$) and had the highest temperature ($\sim 700 \text{ K}$).

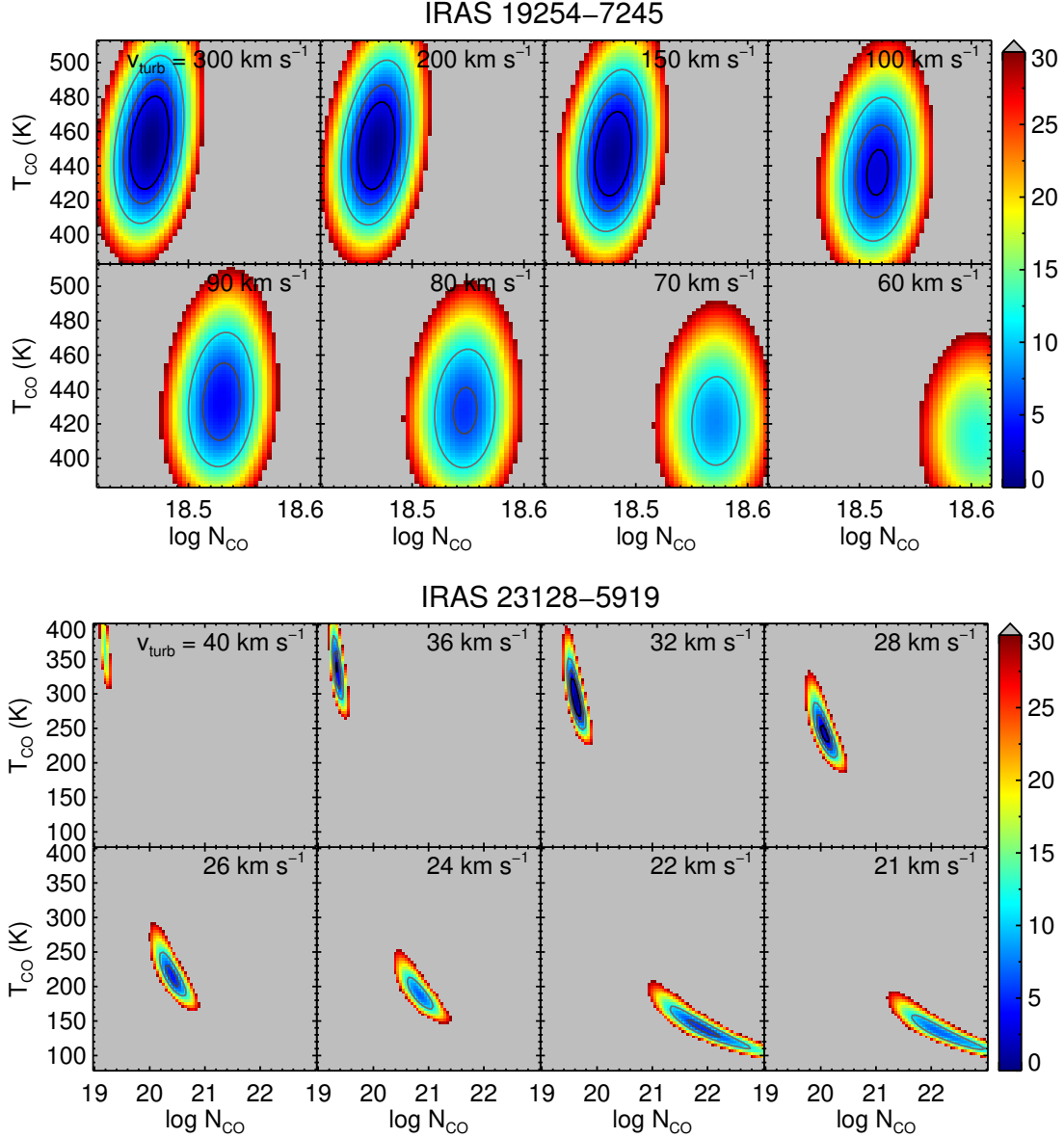


FIG. 12.— (Continued)

Although the *AKARI* observation used in this work did not spatially resolve the two nuclei, we assume that the contribution from the SE nucleus at around $4.67 \mu\text{m}$ is negligible as well as that at $2.2 \mu\text{m}$, as SE is also much fainter in mid-IR wavelengths (Soifer et al. 2000). Our best-fitting column density, $N_{\text{CO}} = 10^{19.3} \text{ cm}^{-2}$, and temperature, $T_{\text{CO}} = 417 \text{ K}$, were ~ 7 times larger and ~ 1.3 times higher, respectively, than those of the most prominent component of S13. Below, we discuss the source of this inconsistency.

The *AKARI* spectrum used in this study and the Subaru spectrum used in S13 have quite different wavelength coverages. The former covered only the *R*-branch, while the latter, which was limited by the atmospheric window, covered an almost opposite wavelength range corresponding to the *P*-branch. Thus, the discrepancy in the column densities found from the *R*- and *P*-branches can be attributed to the absorption profile becoming “asymmetric” and deviating from the current model prediction. Although it is possible that the effects mentioned in Section 5.1 can cause such an asymmetric absorption profile, these effects are weak to explain the difference.

We propose that the most plausible interpretation for the discrepancy is that S13 underestimated the continuum level in the calculation of the equivalent widths. As the Subaru spectrum used by S13 did not cover featureless wavelength regions, the authors determined the continuum level under the assumption that high-intensity peaks correspond to zero-absorption intensities. However, this determination is not trivial. The absorption depth in the Subaru spectrum coincides with that observed with *AKARI* if the actual continuum level is higher than that adopted by S13 by 30%. In this case, the equivalent width of each rotational line increases, and the excitation temperature of the dominant component obtained from the population diagram becomes 480 K. This change follows the trend in the discrepancy

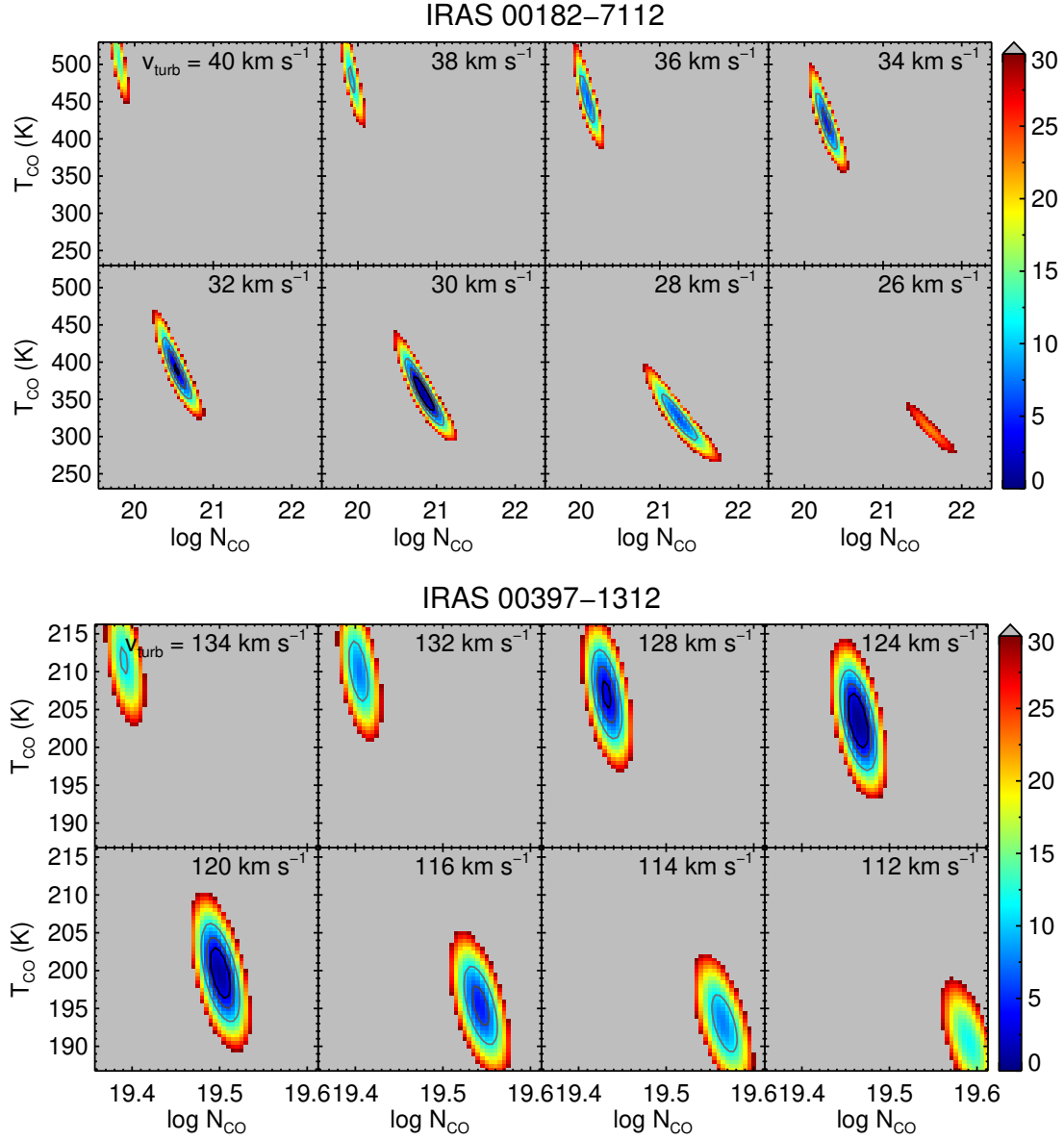


FIG. 12.— (Continued)

between our analyses and those of S13. To confirm this explanation, we require a seamless spectrum that continuously covers both the *P*- and *R*-branches. Such a spectrum can be acquired using the upcoming *James Webb Space Telescope*.

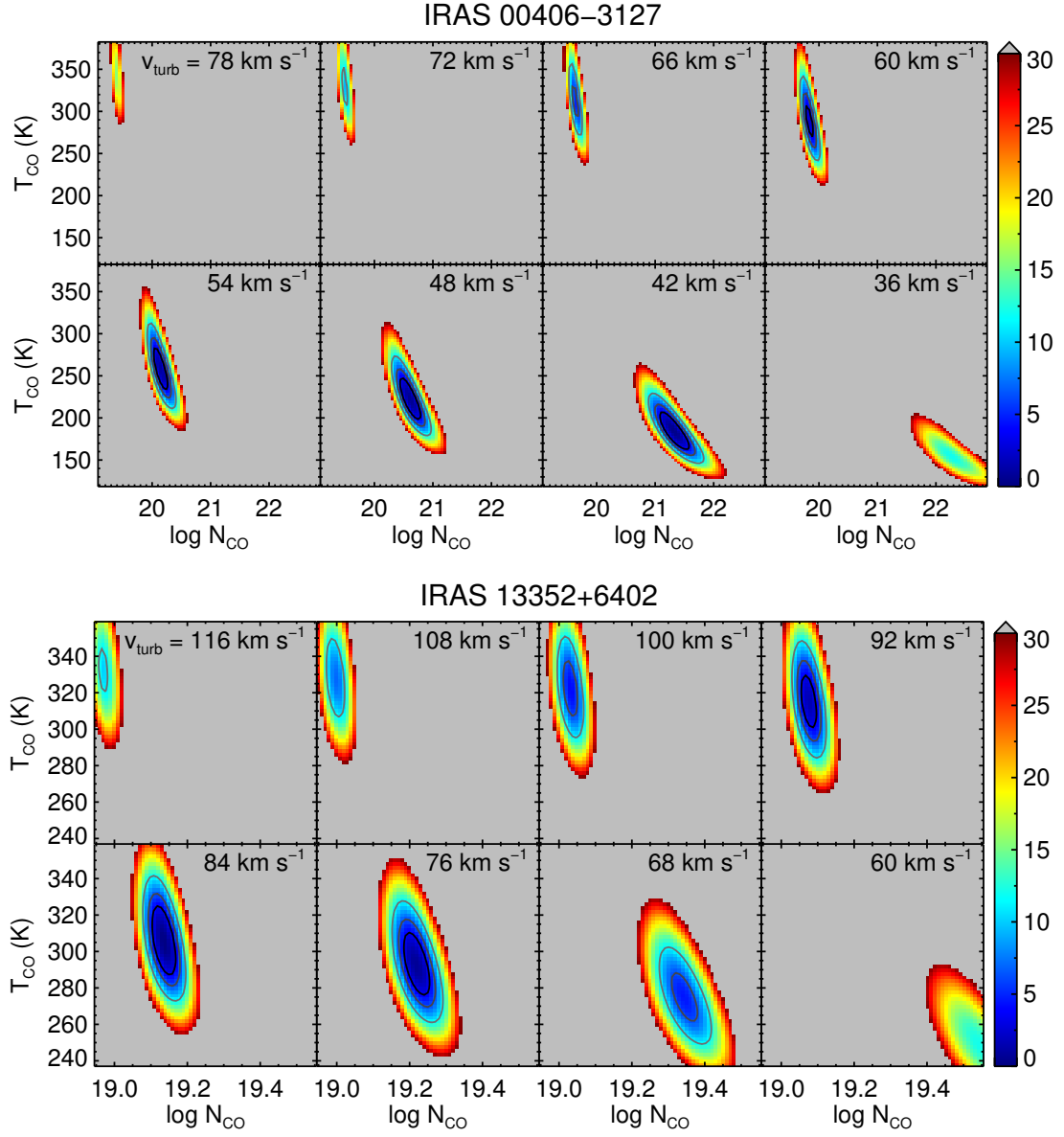


FIG. 12.— (Continued)